Transforming Li_3PS_4 via Halide Incorporation: A Path to Improved Ionic Conductivity and Stability in All-Solid-State Batteries

*Tej P. Poudel, Michael J. Deck, Pengbo Wang, Yan-Yan Hu**

T.P. Poudel, M.J. Deck, P. Wang, Dr. Y.-Y. Hu
Chemical Science Laboratory
Department of Chemistry and Biochemistry
95 Chieftan Way, Tallahassee, FL 32306, USA
E-mail: yhu@fsu.edu; hu@chem.fsu.edu

T.P. Poudel, Dr. Y.-Y. Hu
The Graduate School, Florida State University
Materials Science and Engineering
2005 Levy Ave., Tallahassee, FL 32310, USA
E-mail: yhu@fsu.edu

Dr. Y.-Y. Hu
Center of Interdisciplinary Magnetic Resonance
National High Magnetic Field Laboratory
1800 East Paul Dirac Drive, Tallahassee, FL 32310, USA
E-mail: yhu@fsu.edu

Orcid:
Tej P. Poudel: 0000-0003-4787-5739
Michael J. Deck: 0000-0001-6439-8634
Pengbo Wang: 0000-0002-5740-6912
Yan-Yan Hu: 0000-0003-0677-5897

Keywords: solid electrolytes; local disorder; solid-state NMR; energy storage; stability; batteries

Abstract

To enhance Li^+ transport in all-solid-state batteries (ASSBs), harnessing localized nanoscale disorder can be instrumental, especially in sulfide-based solid electrolytes (SEs). In this investigation, we delve into the transformation of the model SE, Li_3PS_4, via the introduction of LiBr. ^{31}P NMR unveils the emergence of a glassy PS_4^{3-} network interspersed with Br^-. ^6Li NMR corroborates swift Li^+ migration between PS_4^{3-} and Br^-, with increased Li^+ mobility indicated by NMR relaxation measurements. A more than four-fold enhancement in ionic conductivity is observed upon LiBr incorporation into Li_3PS_4. Moreover, a notable decrease in activation energy underscores the pivotal role of Br^- incorporation within the anionic lattice, effectively reducing the energy barrier for ion conduction and transitioning Li^+ transport dimensionality from 2D to 3D. The compatibility of Li_3PS_4 with Li metal is improved through LiBr incorporation, alongside an increase in critical current density from 0.34 mA cm^{-2} to 0.50 mA cm^{-2}, while preserving the electrochemical stability window. ASSB cells with $3Li_3PS_4$:LiBr as the SE and TiS_2 as the active electrode material showcase robust high-rate and long-term cycling performance. These findings collectively indicate the potential of lithium halide incorporation as a promising avenue to enhance the ionic conductivity and stability of SEs.

1. Introduction

Rechargeable lithium-ion batteries (LIBs) represent a revolutionary technological advancement, attributed to their characteristics such as high energy and power density, long cycle life, and versatility.[1] LIBs have found widespread use in various applications from consumer electronics to electric vehicles to renewable energy storage, and enabled the development of new technologies. However, the use of flammable organic solvents in the current generation of LIBs often leads to safety hazards resulting from dendrite formation and thermal runaway.[2] In addition, these liquid electrolytes are not typically compatible with Li-metal anodes. [3] To mitigate safety hazards and increase energy densities, high-performance all-solid-state batteries (ASSBs) hold a promising future in energy storage by overcoming the current challenges of LIBs.[3,4] The advancement of ASSBs is intricately linked to the progress in developing solid electrolytes (SEs). The use of SEs allows for the possible use of a metallic lithium anode,[5,6] wide temperature operational range,[7–11] and enhanced safety.[12–14] The following properties are favorable in the development of superionic conductors as electrolytes in ASSLBs: (1) ionic conductivity > 1 mS cm^{-1} with low

activation energy, (2) compatibility with electrodes over a wide electrochemical window, (3) low electronic conductivity, (4) chemical, mechanical, and thermal stability, (5) facile processing, (6) scalability, and (7) sustainability.[15]

Various types of SEs are being developed, such as inorganic, polymer, and inorganic-polymer composite electrolytes.[16] Inorganic lithium SEs can be categorized into sulfide, oxide, and halide SEs, each with advantages and disadvantages. Sulfide SEs hold great promise due to their ionic conductivity being comparable to that of liquid electrolytes (≥10 mS cm^{-1}).[17] However, their suitability is compromised by insufficient stability when paired with Li metal anodes and current commercial cathodes. Glass-ceramic composite electrolytes are gaining interest due to their high ionic conductivity, facile synthesis, and improved mechanical properties.[9] Among the glass-ceramic SEs, β-Li_3PS_4 has attracted special attention due to its stability against Li. However, it exhibits low ionic conductivity on the order of 10^{-4} S cm^{-1}.[18,19,20] Recent improvements in the conductivity of Li_3PS_4 have been achieved via the introduction of local disorder on the atomic-[17,21,22] as well as nano-scale by producing Li_3PS_4-composite SEs.[9,10,23,24]

Recent studies have shown that halogen anion incorporation into thiophosphate electrolytes can significantly increase Li^+ conductivity and improve chemical stability (i.e., combine the intrinsic advantages of halides with sulfides).[17,25–27] For example, reports on Li_3PS_4 with 30 mol% LiI have shown an increase in ionic conductivity along with an increase in critical current density (CCD).[24,26,28] Furthermore, long-term mechanochemical milling of Li_3PS_4 with LiBr followed by ampule sintering was reported to increase the conductivity and air stability of Li_3PS_4.[29]

In this project, Li_3PS_4 and Li_3PS_4-LiBr composite solid electrolytes (SEs) are prepared via the solid-state mechanochemical milling (high energy ball milling) method. The local structural environments of SEs are characterized using solid-state NMR and variable-temperature EIS. With the incorporation of LiBr in Li_3PS_4, a significant increase in ionic conductivity, critical current density (CCD), and compatibility against Li metal is obtained with no significant change in the electrochemical stability window. Galvanostatic cycling of solid-state half-cells using TiS_2 as the cathode active material (CAM) delivers improved cyclability of cells with LiBr-modified Li_3PS_4 compared to pristine Li_3PS_4. This work provides an in-depth fundamental understanding of changes in the local structures and Li^+ dynamics upon LiBr incorporation into Li_3PS_4 and demonstrates its viability in ASSBs.

2. Results and Discussion

2.1. Structure

The synthesis process of Li_3PS_4-LiBr is shown in the schematic diagram **Figure S1** and uses a solid-state synthesis method (see methods). Li_3PS_4 SEs were prepared with various hours (2.5 h - 10 h) of ball milling time followed by pellet sintering at 210 ℃ for 2 h. Li_3PS_4-LiBr SEs were then prepared by ball-milling the corresponding Li_3PS_4 with LiBr in 3:1 molar ratio for 2.5 h. Li_3PS_4 can crystallize in the γ-phase, which has relatively low Li^+ conductivity, or into the β-phase (**Figure 1b**), which has higher Li^+ conductivity.[9] The phase transition to β-phase is reported at a temperature higher than 190 ℃ for Li_3PS_4, which is further aided by high-energy ball milling, which mimics quenching.[9,30] The ionic conductivity of the β-phase is enhanced in comparison to the γ-phase by the emergence of octahedral sites for Li-ions migration due to the variation of the S^{2-} position into the zig-zag arrangement from the ordered arrangement in the γ-phase.[30] The synthesized pristine compound, β-Li_3PS_4, exhibits the Pnma space group and is comprised of $(PS_4)^{3-}$ tetrahedral units with three different lithium sites, Li1, Li2, and Li3 (**Figure 1a**), corresponding to the 8d, 4b, and 4c Wyckoff positions, respectively. Bulk structure characterization of the samples was performed with powder X-ray diffraction (PXRD) and is shown in **Figure 1b**. Li_3PS_4-BM-7.5h and 3(Li_3PS_4-BM-7.5h):LiBr are chosen as model systems for the reasons described below and denoted as Li_3PS_4 and $3Li_3PS_4$:LiBr hereafter, respectively. The PXRD pattern of the Li_3PS_4 confirms the presence of a low crystalline (glassy) β-Li_3PS_4 phase.[31] Whereas the PXRD pattern of composite samples is observed to be amorphous without any significant diffraction intensity, except the residual LiBr phase. The broad peak around 12° in the XRD of $3Li_3PS_4$:LiBr, is likely from the non-crystalline electrolyte phase, consistent with the broad resonance observed from ^{31}P NMR (**Figure 2**). Scanning electron microscopy was utilized to examine the morphology of $3Li_3PS_4$:LiBr and Li_3PS_4 and evaluate the impact of the second-stage ball milling step on grain size. **Figure S2** shows that $3Li_3PS_4$:LiBr and Li_3PS_4 exhibit a similar size distribution ranging from 0.5 μm to 2 μm. Moreover, because of the glass-ceramic nature of these thiophosphate SEs, solid-state NMR is necessary for accurate structural characterization due to its ability to probe the short- to medium-range structures.[32]

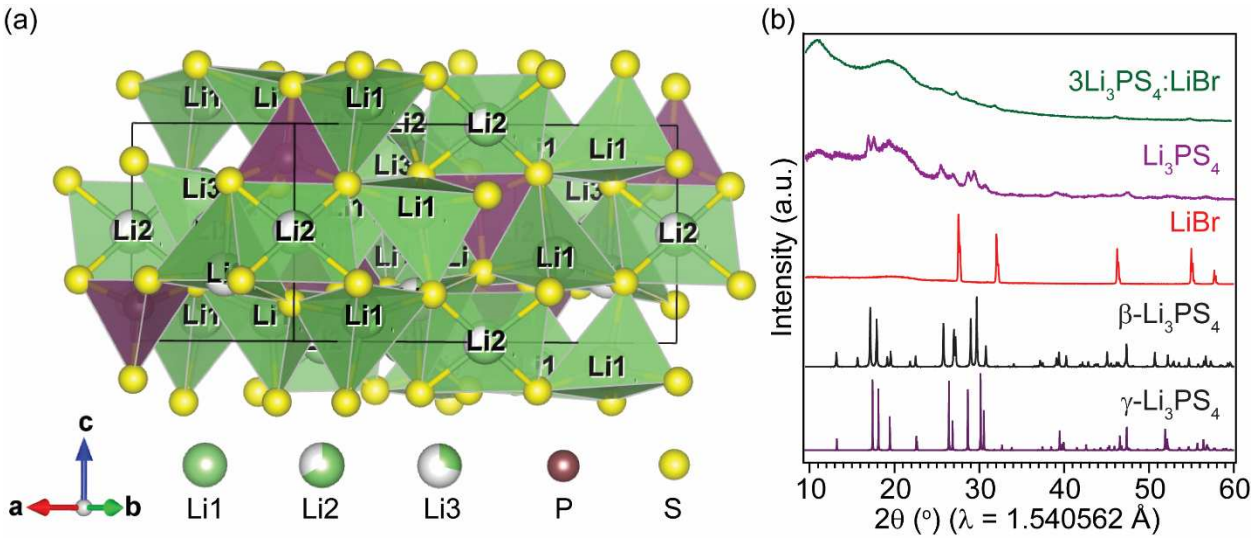

Figure 1. (a) Crystal structure of β-Li_3PS_4 (ICSD #180319). (b) PXRD patterns of Li_3PS_4, LiBr, and $3Li_3PS_4$:LiBr. The XRD patterns of β-Li_3PS_4 (ICSD #180319) and γ-Li_3PS_4 (ICSD #180318) are shown as a reference. Broad Kapton film background at approximately 20°.

To examine the effect of LiBr incorporation on local structural environments, ^{6}Li, and ^{31}P MAS NMR experiments are performed.[32] As shown in **Figure 2a**, the ^{6}Li signal of Li_3PS_4 resides at 0.9 ppm. A shoulder around 1.1 ppm is observed, accounting for 18% of the total Li amount and likely from γ-phase (quantification shown in **Table S1**). After the introduction of LiBr into the Li_3PS_4 structural framework, the ^{6}Li signals shift to 0.5 ppm, indicating further changes to the Li environments. Solid LiBr has a ^{6}Li NMR shift of ~-1.9 ppm; Li^+ ions rapidly shuffling between $(PS_4)^{3-}$ and Br^- during transport will have an apparent shift between 0.9 ppm and -1.9 ppm if the shuffling rate is much higher than the NMR time scale. The exact value depends on the relative ratio of $(PS_4)^{3-}$ and Br^- and the residential time of Li^+ on them. Meanwhile, both Li_3PS_4-LiBr SEs with varying ball milling (BM) times of Li_3PS_4, namely, 3(Li_3PS_4-BM-7.5):LiBr and 3(Li_3PS_4-BM-2.5):LiBr, exhibit a narrower line shape than that of Li_3PS_4, indicating increased Li^+ motion in the $3Li_3PS_4$-LiBr SEs.[33] The signal of the 3(Li_3PS_4-BM-2.5):LiBr sample shows a small peak around 1.4 ppm, attributed to the non-conductive $Li_4P_2S_6$.[34] However, this peak is not present in the 7.5 h sample, implying a longer ball milling time for the preparation of the Li_3PS_4 can remove $Li_4P_2S_6$.

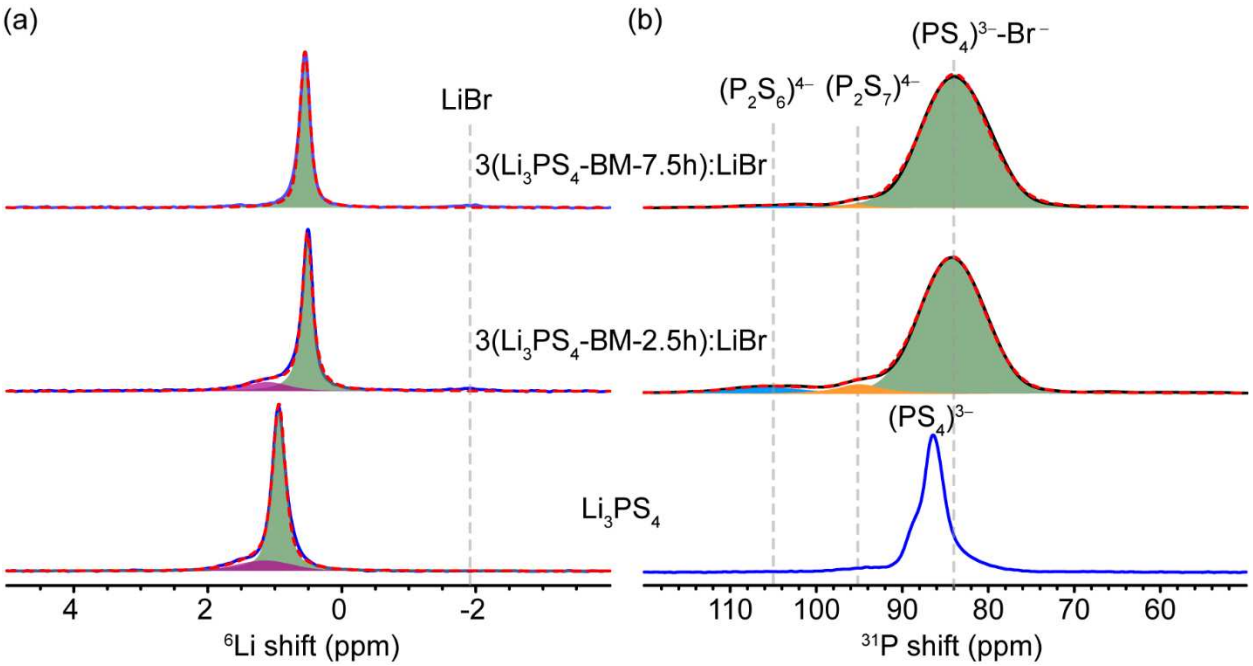

Figure 2. (a) ^{6}Li and (b) ^{31}P MAS NMR spectra of Li_3PS_4, 3(Li_3PS_4-BM-2.5h):LiBr, and 3(Li_3PS_4-BM-7.5h):LiBr.

Table 1. ^{7}Li spin-lattice relaxation time (T_1) of Li_3PS_4, 3(Li_3PS_4-BM-7.5h):LiBr, and 3(Li_3PS_4-BM-2.5h):LiBr.

Sample	^{7}Li T_1 [s]
Li_3PS_4	1.93
3(Li_3PS_4-BM-7.5h):LiBr	1.72
3(Li_3PS_4-BM-2.5h):LiBr	1.99

The incorporation of LiBr significantly changes the nature of the $(PS_4)^{3-}$ framework as seen from the ^{31}P NMR (**Figure 2b**). Compared with Li_3PS_4, the ^{31}P resonances of Li_3PS_4-LiBr SEs become significantly broader and shift to lower ppm, which reflects the reduction of the crystallinity, echoing the results from powder X-ray diffractions and the introduction of Br^-. Li_3PS_4 begins with a major β-$(PS_4)^{3-}$ phase at 86 ppm and a minor γ-$(PS_4)^{3-}$ signal at around 88 ppm,[35] while in 3(Li_3PS_4-BM-7.5h):LiBr and 3(Li_3PS_4-BM-2.5h):LiBr samples, the major resonance is from the glassy $(PS_4)^{3-}$-Br^- unit around 84 ppm.[36] In addition, two minor resonances

at 95 ppm and 106 ppm are observed in 3(Li_3PS_4-BM-2.5h):LiBr, attributed to $(P_2S_7)^{4-}$ and $(P_2S_6)^{4-}$. $Li_4P_2S_6$ is a common and low-conducting impurity; the 3(Li_3PS_4-BM-7.5h):LiBr shows no sign of $Li_4P_2S_6$.[25] ^{7}Li spin-lattice relaxation time (T_1) is a sensitive probe to Li^+ dynamics. **Table 1** shows that 3(Li_3PS_4-BM-7.5h):LiBr has a shorter T_1 than Li_3PS_4, which indicates faster Li-ion motion.[37,38] The slightly longer T_1 of 3(Li_3PS_4-BM-2.5h):LiBr is an average value of the conductive phase and non-conductive impurities as revealed in both ^{7}Li and ^{31}P NMR spectra**.**

Further characterization of the P-S bond nature is carried out using Raman spectroscopy. Raman spectroscopy is a short-range structural tool that can be used for determining thiophosphate polyhedrons and a useful complement to solid-state NMR which can probe both short- and intermediate-range structures. The Raman shift of the $(PS_4)^{3-}$ peak for all samples is observed at around 423 cm^{-1}.[36] The presence of $(P_2S_7)^{4-}$ impurities and low conducting $(P_2S_6)^{4-}$ impurities is observed for the sample with low overall ionic conductivity (**Figure 3)**.[39] Whereas the sample ball-milled for 7.5 h exhibits no signs of the impurity peaks.[39] This is consistent with ^{31}P NMR results. The reduction of impurity is likely responsible for the increase in conductivity for the longer ball-milled electrolyte, 3(Li_3PS_4-BM-7.5h):LiBr.

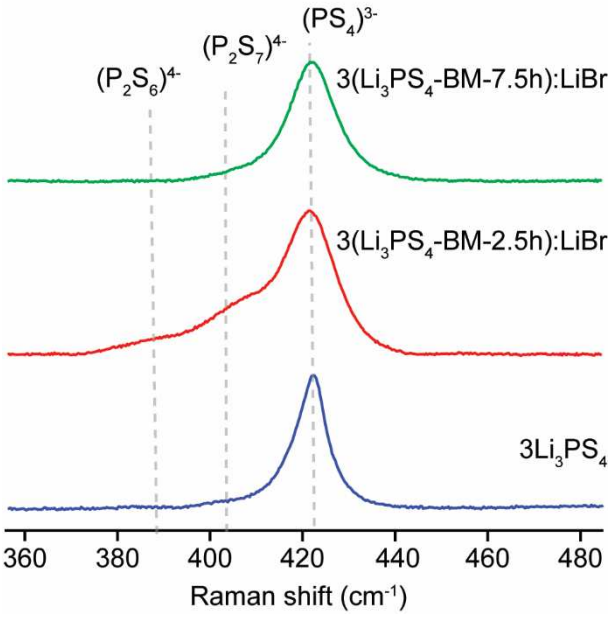

Figure 3. Raman spectra of Li_3PS_4, 3(Li_3PS_4-BM-7.5h):LiBr, and 3Li_3PS_4-BM-2.5h:LiBr.

2.2. Fast-ion Conduction in Li_3PS_4 with LiBr Incorporation

The electronic conductivity of Li_3PS_4-BM-7.5h and the corresponding $3Li_3PS_4$:LiBr was measured by using the DC polarization method as shown in **Figure S3**. Very low electronic conductivities of 1.65 x 10^{-9} S cm^{-1} for Li_3PS_4 and 1.04 x 10^{-9} S cm^{-1} for $3Li_3PS_4$:LiBr is measured at 25 °C. To investigate the effect of the introduction of LiBr on Li^+ transport, variable-temperature EIS measurements of the SEs are performed, and the representative 25 °C Nyquist plots are shown in **Figure S4**.

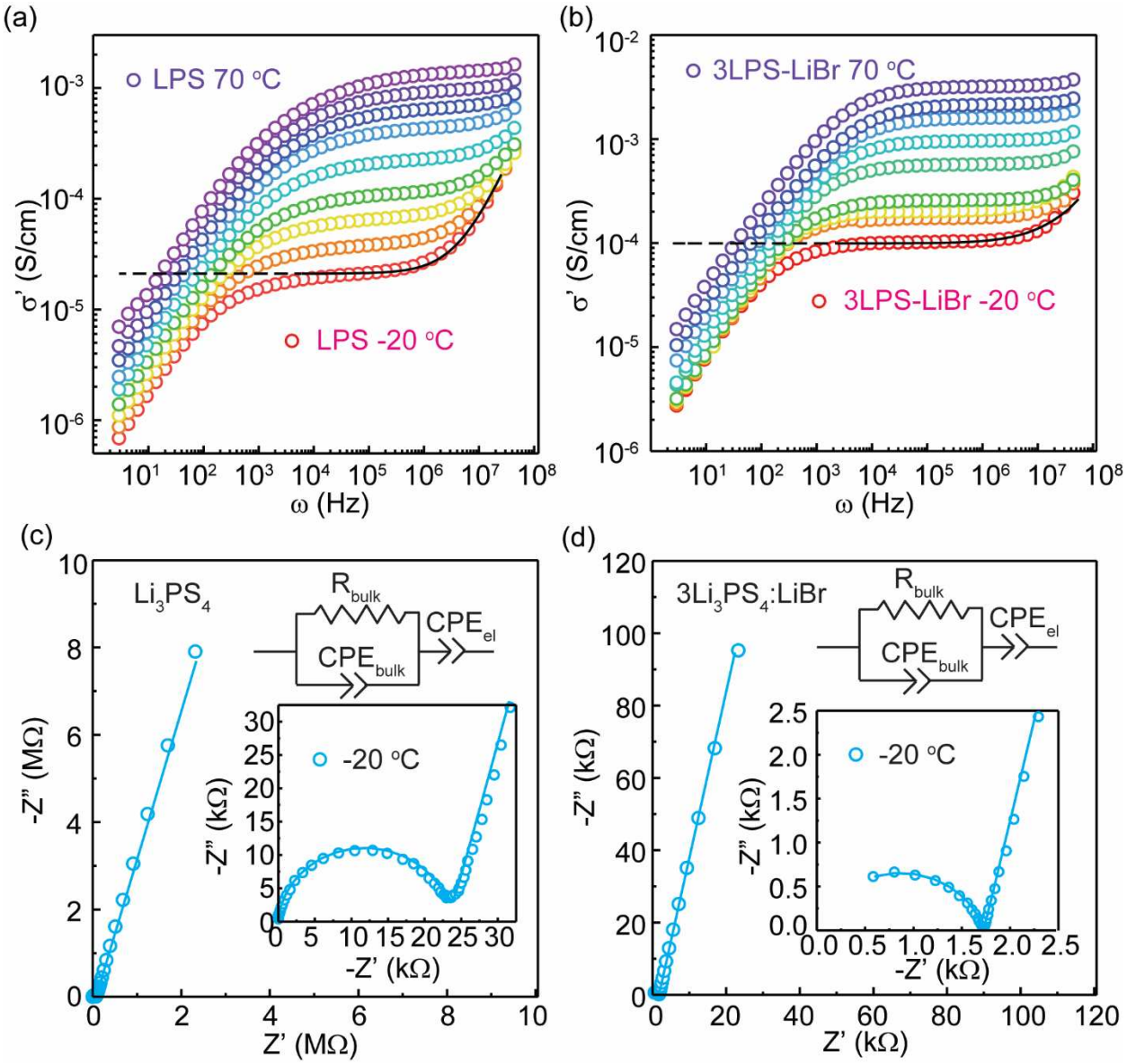

Figure 4. (a), (b) Conductivity isotherms and the Jonscher power law fitting for the isotherm at -20 °C, for Li_3PS_4 and $3Li_3PS_4$:LiBr, respectively. (c) Nyquist plot at -20 °C with equivalent circuit

fitting (inset) for Li_3PS_4 (d) Nyquist plot at -20 °C with equivalent circuit fitting (inset) for $3Li_3PS_4$:LiBr.

Variable-temperature EIS measurements were performed from -20 ^{0}C to 70 ^{0}C. From the conductivity isotherms, only one frequency-independent direct current (DC) plateau is observed (**Figure 4a,b**) which suggests the macroscopic Li^+ conduction involves the bulk process.[40] To further confirm this, the equivalent circuit was fitted with the (RQ)Q type for the Nyquist plots at -20 ^{o}C (**Figure 4c,d**) and only one semicircle is detected, as expected, which confirms the macroscopic Li^+ conduction only involves the bulk process. The conductivity was calculated from the equivalent circuit model fits using the following equation,

$$\sigma_{DC} = \frac{L}{R \times A} \qquad (1)$$

where *L* and *A* are the thickness of the pellet and surface area of the blocking electrode respectively, and *R* is the value of resistance extracted from the equivalent circuit fitting. For the Li_2S-P_2S_5 system, increasing the ball milling time increases the conductivity to 0.29 mS cm^{-1} for the sample milled for 10 h, compared with 0.16 mS cm^{-1} for the sample milled for 2.5 h. This increase in conductivity with longer ball milling time is likely associated with the higher reaction time between Li_2S and P_2S_5 resulting in a β-Li_3PS_4 phase without impurity.[41] With the incorporation of LiBr, a more than four-fold increase in conductivity is observed. The highest conductivity of 1.06 mS cm^{-1} is observed for the composite electrolyte with 7.5 h of ball-milling for the Li_2S-P_2S_5 system. These values align well with the trend from ^{7}Li T_1 discussed above (**Table 1**). **Figure 5a** shows the room temperature ionic conductivity *vs.* the $3Li_2S$:P_2S_5 (first stage) ball milling time and **Figure 5b** shows the Arrhenius plot of the 7.5 hours milled Li_3PS_4 and corresponding $3Li_3PS_4$:LiBr SEs extracted from fitted Nyquist plots at variable temperatures. The Arrhenius-type conductivity **Equation (2)** was used. The Arrhenius-type conductivity equation can be written as

$$\sigma_{DC} T = \sigma_0 \, exp^{-E_{a_{DC}}/k_B T} \qquad (2)$$

where σ_{DC} is the DC ionic conductivity, T is the temperature in K, σ_0 is the Arrhenius perfector, $E_{a,DC}$ is the activation energy, and k_B is the Boltzmann constant.[42] From the Arrhenius relation (**Equation 2**), the conductivity depends on thermal energy, resulting in increased ionic conductivity with temperature. Arrhenius plots for all the prepared samples are shown in **Figure S5** and Arrhenius prefactor (shown in **Figure S6**). EIS analysis of all samples is listed in **Table**

S2. The $E_{a,DC}$ is calculated using the slope of the Arrhenius plots. The $E_{a,DC}$ of the β-Li_3PS_4 sample milled for 7.5 h is 0.38 eV, and it decreases to 0.34 eV upon optimal LiBr incorporation as shown in **Figure 5a,b**. The significant drop in activation energy with the incorporation of LiBr could be due to the increase in local disorder brought by the LiBr incorporation in the Li_3PS_4 system.[43] Local disorder via anion introduction distorts Li^+ site energies and creates a distribution of lithium site energies that allows for facile Li^+ transfer from site to site due to increased site energy overlap between neighboring Li-ions.[44] Another potential reason for the increase in ionic conductivity can be a change in the dimensionality of Li^+ transport from 2D to 3D, as has been predicted computationally upon optimal local disorder in Li_3PS_4[45] as well as experimentally.[46] To experimentally determine this, we further analyze the conductivity isotherms (**Figure 4a,b**) determined from VT-EIS and fit with the Jonscher power law, $\sigma' = \sigma_{DC} + A\omega^n$, where σ' is the AC conductivity, σ_{DC} is the DC ionic conductivity, A is the alternating current coefficient, and n is the power law exponent.[46–48] n is an empirical indicator of the effective dimensions of ion conducting pathways for Li^+ transport. A value of $n > 0.7$ indicates 3D conduction within the SE.[49] The fitted n values are listed in **Table 2**. The value of n for Li_3PS_4 is 0.63, which indicates a 2D ion conductor and aligns well with that from the previous reports.[49,50] Furthermore, a n value of 0.82 for $3Li_3PS_4$:LiBr indicates 3D conduction. Therefore, with the incorporation of LiBr into Li_3PS_4, the increase in ionic conductivity and decrease in activation energy is due to the local disorder that is introduced which leads to a "frustrated energy landscape" and prevents Li-ions from being energetically trapped.[44,51,52]

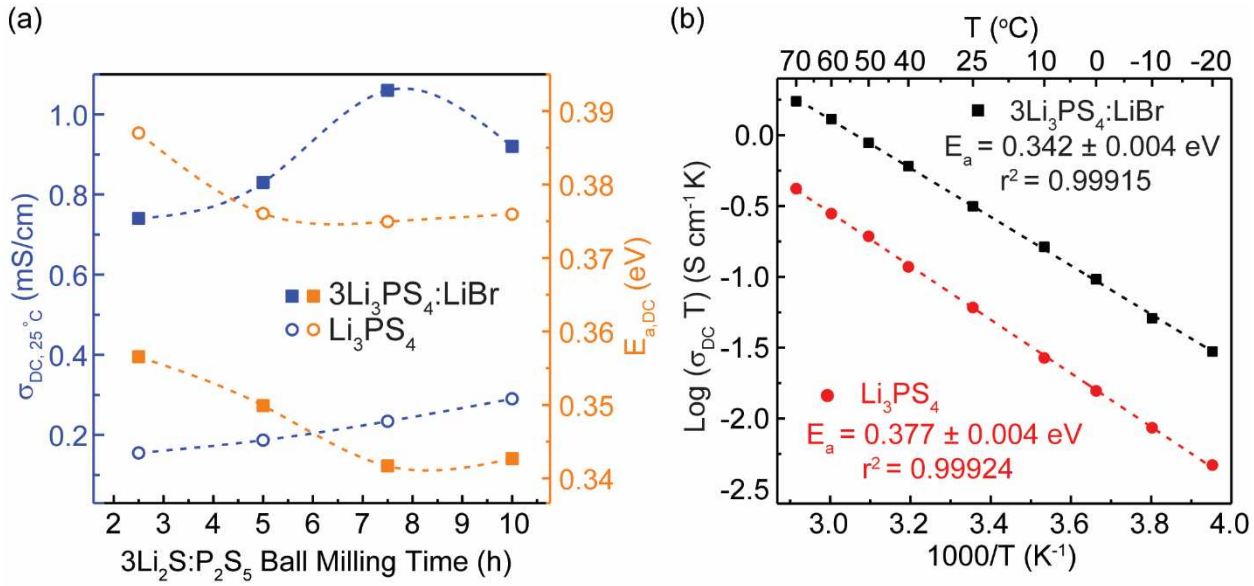

Figure 5. (a) Effect of high-energy ball milling of $3Li_2S:P_2S_5$ on the iconic conductivity and activation energy barriers of the final products: Li_3PS_4 and $3Li_3PS_4$:LiBr (All the composite $3Li_3PS_4$:LiBr were hand milled followed by high energy ball milled for 2.5 hours). (b) Arrhenius plots of ionic conductivity *vs.* temperature (1000/T (K^{-1})) and the extracted activation energies (E_a) for ion transport in Li_3PS_4 and $3Li_3PS_4$:LiBr synthesized with the optimal ball-milling time.

Table 2. EIS analysis of Li_3PS_4 and $3Li_3PS_4$:LiBr

Sample	$\sigma_{DC,\ 25\ ^\circ C}$ [mS cm^{-1}]	E_a [eV]	Log (σ_0) [S cm^{-1} K]	*n*
Li_3PS_4	0.23	0.38	5.20	0.63
$3Li_3PS_4$:LiBr	1.06	0.34	5.22	0.82

2.3. Electrochemical Performance of Li_3PS_4 and $3Li_3PS_4$:LiBr

With the observation of improved ionic conductivity for the SE upon LiBr incorporation, it is important to examine the performance of the SE in battery cells.[53] To understand the stability of the prepared SEs with Li metal, we performed symmetric cycling and critical current density (CCD) measurements on Li_3PS_4 and Li_3PS_4:LiBr SEs. The CCD against lithium metal is the minimum current density below which stable charge-discharge of ASSBs is possible.[54] The CCD

of solid lithium-ion conductors indicates at which current density the cell shorting takes place due to lithium metal penetration or severe surface reaction. A high CCD of the SE is required for high-rate performance ASSBs and it is associated with the power density of the battery.[55] The CCD is measured with Li/SE/Li symmetric cells as shown in **Figure 6a,b.** For the $Li/Li_3PS_4/Li$ symmetric cell the CCD is 0.34 mA cm^{-2}, and the CCD increases to 0.50 mA cm^{-2} for $Li/3Li_3PS_4$:LiBr/Li. The improvement in CCD for $3Li_3PS_4$:LiBr is most likely due to the improved interfacial stability of the electrolyte with Li metal, increase in ionic conductivity, and decrease in electronic conductivity as shown in **Figure S3**.[53] The improved CCD indicates that $3Li_3PS_4$:LiBr will facilitate better fast charging of ASSBs in comparison to pristine Li_3PS_4.

Long-term symmetric cycling is performed at 0.1 mA cm^{-2} for Li/SE/Li cells (**Figure 6c**). The $Li/Li_3PS_4/Li$ symmetric cell fails after ~6 days of cycling at room temperature however $Li/3Li_3PS_4$:LiBr/Li doesn't fail for over 125 days. The smaller increase in voltage over time for the $Li/3Li_3PS_4$:LiBr/Li symmetric cell compared with the $Li/Li_3PS_4/Li$ cell (**Figure 6c**) indicates enhanced interfacial stability and improved compatibility of $3Li_3PS_4$:LiBr with Li-metal.

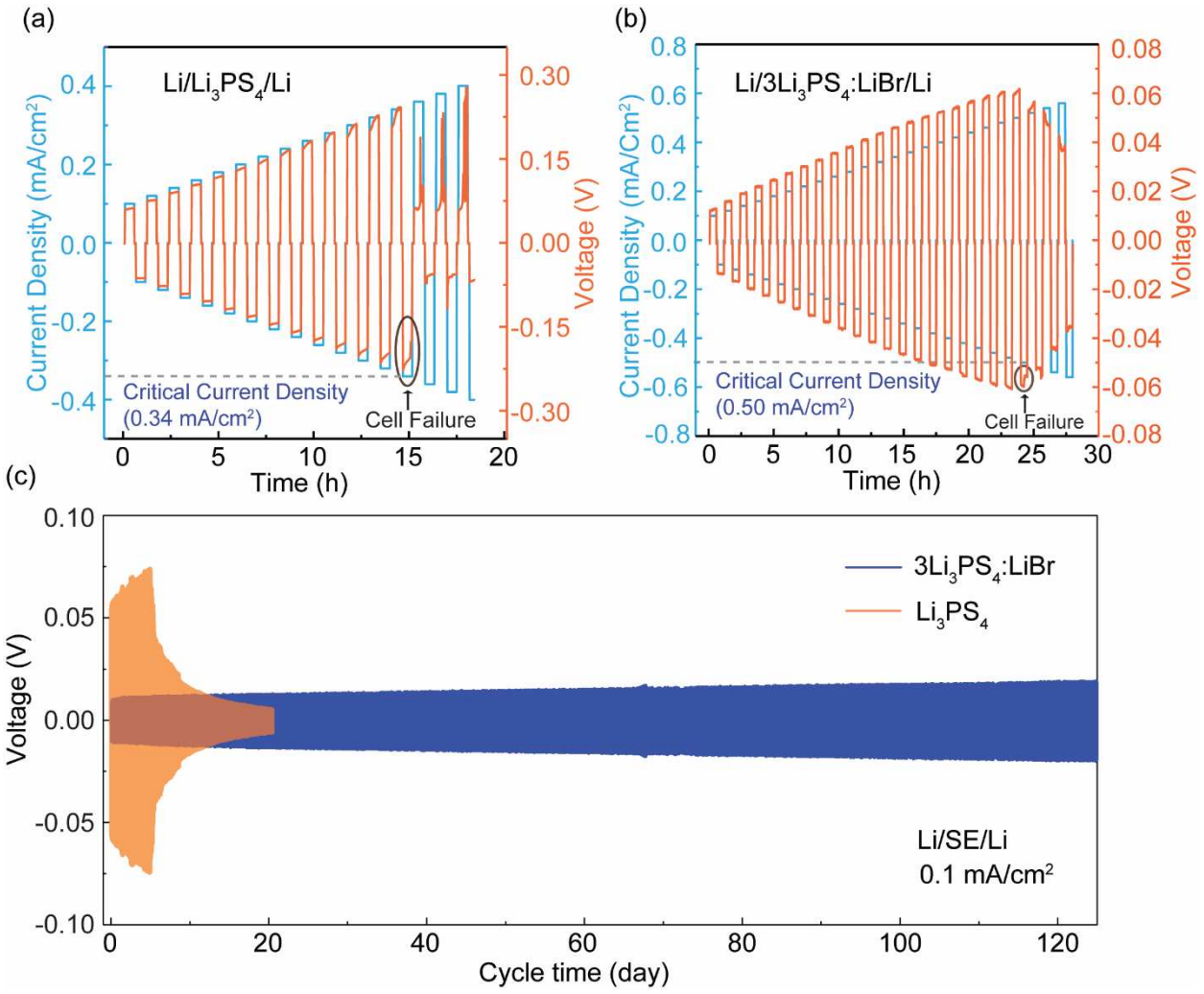

Figure 6. Electrochemical performance of $3Li_3PS_4$:-LiBr as solid electrolytes in Li/SE/Li symmetric cells at 22 °C, compared with Li_3PS_4. (a) critical current density measurement of Li_3PS_4 (b) critical current density measurement of $3Li_3PS_4$:-LiBr, (c) long-term cycling performance of Li_3PS_4 and Li_3PS_4:LiBr at 0.1 mA cm^{-2}.

Accessing the electrochemical stability window of the prepared high-conductive electrolytes and the pristine lithium thiophosphate is important for evaluating the electrochemical performance of the SE.[56] The electrochemical potential window is the potential range in which the electrolytes and their components are not reactive and shows inertness towards the oxidation and reduction process.[57] In other words, the potential window is the voltage range where no Li^+ is lost by the SE.[58] The traditional cyclic voltammetry (CV) measurement with stainless steel as the blocking electrode does not reflect the real voltage window of SEs and usually overestimates the potential window;[56,59] accordingly the Li_3PS_4 and $3Li_3PS_4$:LiBr CV cells were assembled

using Li-In as the anode, SE separator, and a 3SE:C (mass ratio) composite cathode, which is often used in literature of SEs.[60–64] Carbon is used here as an electronic conductive medium in a composite cathode which allows a more accurate measurement of degradation current due to its higher surface area and sensitive detection of degradation current.[56,60–62,65]

The stability window of Li_3PS_4 SEs was estimated computationally and found to be from 1.11 V - 1.77 V *vs.* Li-In.[45,66] **Figure 7a** shows the comparison of the cyclic voltammogram of Li_3PS_4 and $3Li_3PS_4$:LiBr for the first two cycles. During the initial cycle, an onset of cathodic peak around ~1.8 V *vs* Li-In is indicative of the probable formation of S_x^{2-} from S_x (such as the generation of Li_2S). This may be attributed to the existence of unreacted sulfur within the electrolyte.[43,62,67] Commencing from the second cycle onward, the sulfur reduction peak is no longer evident, as depicted in **Figure S7**. $(PS_4)^{3-}$ oxidation (starting at ~2.2 V *vs* Li-In) is prominent in the first anodic sweep and it decreases significantly for subsequent cycles (see **Figure S7**), which can be attributed to the formation of passivation layers.[56] The CV demonstrates the preservation of the stability window, evidenced by the same redox and oxidation voltage onset of the peaks for both anodic and cathodic sweep. $3Li_3PS_4$:LiBr shows a smaller oxidation and reduction current than pristine Li_3PS_4, indicating reduced oxidation and reduction reactions for $3Li_3PS_4$:LiBr, thus improved electrochemical stability.

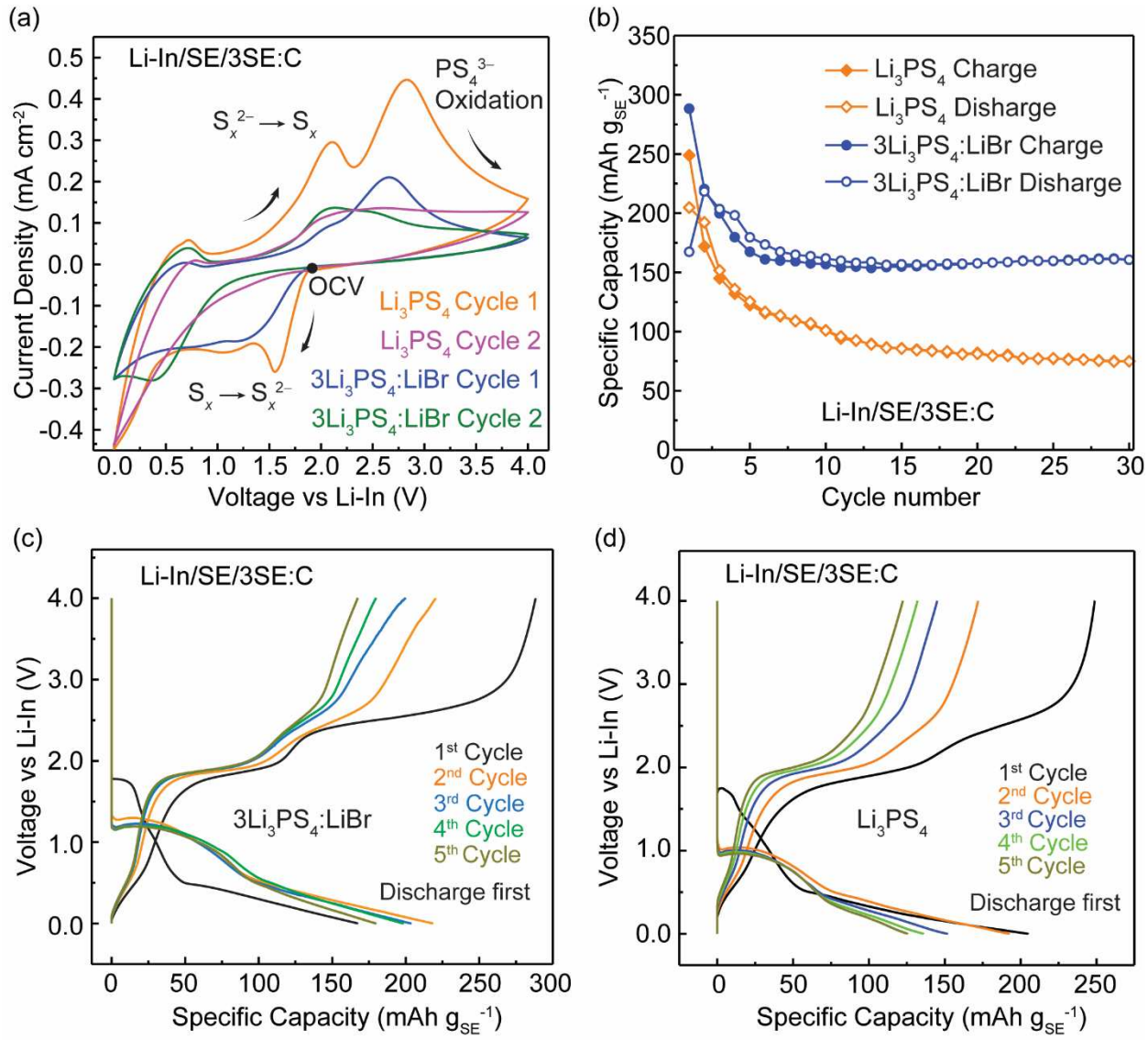

Figure 7. (a) Cyclic voltammograms of Cycles 1 and 2 for Li_3PS_4 and $3Li_3PS_4$:LiBr carbon-containing cells using a scan rate of 0.2 mV s^{-1}. See Supplemental Data (**Figure S7**) for voltammograms of Cycles 1 – 3. (b) Room-temperature capacity *vs.* cycle number. (c) Selected voltage profiles of Cycles 1 – 5 of the Li-In/$3Li_3PS_4$:LiBr/3($3Li_3PS_4$:LiBr):C cell. (d) Selected voltage profiles of Cycles 1 – 5 for Li-In/Li_3PS_4/$3Li_3PS_4$:C cell. The current density used is 0.064 mA cm^{-2}.

Since the bulk SE is not at equilibrium during CV due to the fast scan rates used, in addition to low interfacial contact with the stainless steel current collector,[63] we performed galvanostatic cycling of the carbon composite cells to further examine the stability[62] and evaluate the intrinsic redox nature of sulfide SEs. The Li_3PS_4 and $3Li_3PS_4$:LiBr carbon composite cells (identical to the

one used for CV) were cycled galvanostatically and the corresponding capacities over 30 cycles are shown in **Figure 7b** with the voltage profile shown in **Figure 7c,d**. From the galvanostatic cycling results, we can observe the noticeable capacity gain for both cells at ~1.8V for the 1st discharge due to the possible sulfur redox reaction (**Figure 7c,d**) also observed in the CV in **Figure 7a**. The voltage profile also aligns with the CV for the subsequent cycles; no capacity gain is observed at ~1.8 V, which could be because the sulfur impurities are likely consumed due to redox reactions indicating that no reversible capacity is generated from the elemental sulfur → Li_2S. The significant capacity gain at ~1.0 V *vs.* Li-In after the first cycle can be attributed to the partially reversible SE lithiation/reduction[45] which is also observed in the CV measurement. The cathodic peak at ~0.6 V *vs.* Li-In can be assigned to the reduction (lithiation) of reversible redox product, P, to Li_3P.[43,45,61] On the other hand the first peak in the anodic scan appears at approximately 0.5 V *vs.* Li-In which can be assigned to the oxidation of reduced phosphorous species.[43] The significant peak, located around ~2 V *vs*. Li-In, is attributed to the oxidation process of decomposed components.[57]

This potentially indicates the reaction between Li_2S and Li_xP, leading to the creation of lithium thiophosphate glasses (including thiophosphate polyhedrons), a phenomenon observed in other thiophosphate SEs.[43,56,60] This reaction is highly reversible and shows a stable cycling performance as shown in **Figure 7c,d**.[56] A comparison of the differential capacity (**Figure S8**) shows a similar redox behavior for both Li_3PS_4 and $3Li_3PS_4$:LiBr SEs. The obtained stability window is ~1.0 V to 2.2 V *vs.* Li-In for both Li_3PS_4 and Li_3PS_4-LiBr, which is larger than the computationally predicted limit (1.11 V - 1.77 V *vs.* Li-In).[45]

Notable capacity is generated from SE redox and the redox products based on galvanostatic cycling of the 3SE:C composite cathode cell; this is beneficial if it occurs in the voltage window for ASSB operation and is reversible.[60,61,68] The galvanostatic cycling of the Li_3PS_4 carbon-composite cell shows a higher first discharge capacity of 203 mAh g_{SE}^{-1} than the $3Li_3PS_4$:LiBr cell (165 mAh g_{SE}^{-1}). However, the first charge capacity of the $3Li_3PS_4$:LiBr carbon-composite cell is observed to be higher than that of the Li_3PS_4 carbon-composite cell. This could be because of the increase in ionic conductivity upon LiBr incorporation in Li_3PS_4 giving rise to a greater amount of the capacity-generating redox reactions that occur due to the improved reaction kinetics. Notably, for the initial cycle, PS_4^{3-} oxidation at high voltage contributes to additional capacity upon charge due to the formation of a passivation layer. This in turns decreases the subsequent charge capacities

resulting from the stable passivation layer. For the 2nd cycle, $3Li_3PS_4$:LiBr shows an increase in discharge capacity to 223 mAh g_{SE}^{-1}. The capacity increase could be caused by the redox activity of decomposed products created during the first cycle.[60] During the 2nd charge, the capacity plateaus assigned to PS_4^{3-} oxidation decreases for both Li_3PS_4 and 3 Li_3PS_4:LiBr cells from the passivation interphase formed, and the capacity decreases to 171 mAh g_{SE}^{-1} and 220 mAh g_{SE}^{-1} from 248 mAh g_{SE}^{-1} and 288 mAh g_{SE}^{-1} respectively. For both cells, part of the measured capacity below 1 V *vs*. Li-In is partially attributed to Li intercalation into the Super P (~ 25 mAh g^{-1}).[69] **Figure 7b** shows that Li_3PS_4 carbon-composite cells have almost half the capacity generated than $3Li_3PS_4$:LiBr carbon-composite cells after 30 cycles.

To further investigate the electrochemical performance of the $3Li_3PS_4$:LiBr electrolyte in ASSBs, half-cells containing Li_3PS_4 and $3Li_3PS_4$:LiBr electrolytes were prepared using TiS_2 as the cathode active material (CAM) and Li-In alloy as the anode. From the Nyquist plots of half-cells at 22 °C and the equivalent circuit model shown in **Figure S9**, the bulk resistance of the SE and the CAM/SE resistance can be extracted (**Table S3**).[70] The CAM/SE resistance is of high importance as it can be indicative of chemical compatibility between the SE (Li_3PS_4 or Li_3PS_4:LiBr) and TiS_2, especially when compared between $2Li_3PS_4$:TiS_2 and $2(3Li_3PS_4$:LiBr):TiS_2 containing half-cells. Accordingly, the CAM/SE resistance for $2Li_3PS_4$:TiS_2 and $2(3Li_3PS_4$:LiBr):TiS_2 containing half-cells is 100 Ω and 191 Ω, respectively - indicating that upon Br introduction the chemical compatibility of Li_3PS_4 with TiS_2 does not change significantly. The galvanostatic cycling was performed at various charge/discharge rates from 0.1 C to 1 C (**Figure 8a**). A Li-In anode is used due to greater stability against SEs and less likely to creep through micropores to cause short circuits.[71] The rate performance of the electrolyte at various charge-discharge rates (0.1 C ~ 0.14 mA cm^{-2}, 0.2 C ~ 0.28 mA cm^{-2}, 0.5 C ~ 0.70 mA cm^{-2}, and 1 C ~ 1.40 mA cm^{-2}) for 5 cycles followed by 35 cycles at 0.1 C using 239 mAh g^{-1} as the theoretical capacity for TiS_2. The associated voltage profiles are shown in **Figure 8b,c.** The Li_3PS_4 cell shows a high initial capacity of around 280 mAh g^{-1} for the 2nd cycle but exhibits 0 mAh g^{-1} capacity at 1 C (**Figure 8a,c)**. While the $3Li_3PS_4$:LiBr cell is more stable and has a capacity of approximately 117 mAh g^{-1} for 1 C and the capacity fading is much lower compared to the Li_3PS_4 cell (**Figure 8)**. The measured 1st cycle capacity for both half-cells is higher than the theoretical capacity of TiS_2 (239 mAh g^{-1}) which is likely due to the reversible SE redox,[72] as observed in the same voltage range of the cycled SE carbon composite cells, in addition to the unknown redox phases

from reactions of the SE and TiS_2.[73] Electronic conductivity measurements of the catholyte show the same trend as the pristine SEs, with the $3Li_3PS_4$:LiBr containing catholyte having a smaller value than the Li_3PS_4 containing catholyte (**Figure S10a**) while retaining the PXRD peaks of TiS_2 (**Figure S10b**). The enhanced rate performance for the Li-In/$3Li_3PS_4$:LiBr /2SE:TiS_2 cell can be attributed to a convergence of the enhanced ionic conductivity, better stability of $3Li_3PS_4$:LiBr *vs* Li metal, improved utilization of cathode active materials,[74] and better redox reversibility of $3Li_3PS_4$:LiBr than that of Li_3PS_4 (**Figure 8b,c** and **Figure S11**).

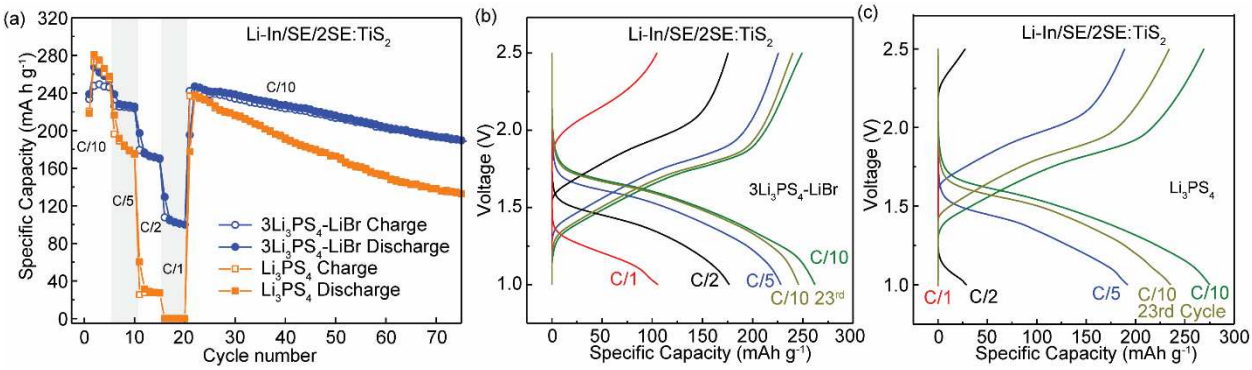

Figure 8. Rate performance cycling of Li-In/$3Li_3PS_4$:LiBr/2SE:TiS_2 and Li-In/Li_3PS_4/2SE:TiS_2 ASSB half-cells at charge discharge rates: C/10, C/5, C/2, and C/1. (a) Capacity *vs.* cycle number. (b) and (c) Voltage profiles of the 2nd cycle at each C-rate for the ASSBs using $3Li_3PS_4$:LiBr, and Li_3PS_4, respectively.

3. Conclusion

With the incorporation of LiBr into β-Li_3PS_4, more than a four-fold increase in conductivity (0.23 mS cm^{-1} to 1.06 mS cm^{-1}) is achieved resulting from the increased Li^+ mobility, decreased activation energy barrier, and expanded dimensionality of Li^+ transport paths from 2D to 3D. The comprehensive structural characterization using XRD (long-range), NMR (intermediate-/short-range), and Raman (short-range) unveils the loss of long-range structural order in $3Li_3PS_4$:LiBr and the partition of Br^- within the PS_4^{3-} anion lattice. Fast Li^+ hoping between Br^- and $(PS_4)^{3-}$ is implied by a single narrow Li NMR resonance. Furthermore, $3Li_3PS_4$:LiBr demonstrates significantly improved critical current density and stability against Li metal. CV measurements show similar reversible redox characteristics for Li_3PS_4 and $3Li_3PS_4$:LiBr, thus no significant change in the electrochemical stability window. $3Li_3PS_4$:LiBr promotes improved rate

performance of ASSBs, retaining a specific capacity of 117 mAh g^{-1} at 1 C for Li-In/3Li_3PS_4:LiBr/2SE:TiS_2, while the ASSB cell using Li_3PS_4 gives 0 mAh g^{-1}. Galvanostatic cell cycling reveals enhanced cyclability and electrochemical performance for long-term batteries using 3Li_3PS_4:LiBr, compared with Li_3PS_4 electrolyte. Enhanced ion transport via anion diversification can be applied to other Li_3PS_4-LiX (X=Cl, I) systems.[17,51,75,76] A diversified anion sublattice prevents Li^+ trapping, yielding increased ion mobility. In addition, the introduced local disorder often leads to a frustrated energy landscape, producing lower energy barriers for ion migration.

4. Experimental Section/Methods

4.1. Materials Synthesis

The Li_3PS_4-LiBr (3Li_3PS_4:LiBr) composite SE was prepared via the high-energy ball milling method. The schematic of the synthesis process is shown in **Figure S1**. The high-energy ball milling technique is leveraged for producing metastable materials that cannot be produced using the thermal equilibrium process.[77] The two-stage ball milling was employed to synthesize the composite SE. A stoichiometric amount of Li_2S (99.98%, Sigma-Aldrich), and P_2S_5 (99%, Sigma-Aldrich) were mixed using mortar and pestle inside an argon-filled glovebox (Vacuum Technology). The solid mixture was then transferred into a zirconia milling jar and two zirconia balls (1 cm diameter) were added followed by vacuum sealing. The first stage of ball milling was carried out for various hours using an SPEX 8000M high-energy miller. The prepared sample was then transferred to a sealed quartz tube inside an MBRAUN glovebox. The precursor powder was heated from room temperature to 210 ℃ at the ramping rate of 1℃ min^{-1}. The sintering temperature was chosen as 210 ℃ because the β-Li_3PS_4 phase forms at a temperature greater than 190 ℃.[41] The sample was heated for 2 hours at 210 ℃ to synthesize the target β-Li_3PS_4.

To incorporate LiBr, as-prepared Li_3PS_4 was then mixed with LiBr at a 3:1 molar ratio in the glovebox using an agate mortar and pestle for 10 mins to form a homogenous mixture. The mixture was then transferred into a zirconia milling jar with two zirconia balls of 1 cm diameter. The second stage high-energy ball milling was carried out for 2.5 h to produce 3Li_3PS_4:LiBr composite SEs. A 6-mm stainless-steel mold was then used to press 50 mg of powder sample at 300 MPa for 10s to obtain a pellet of ~1 mm thickness.

4.2. Materials Characterization

The sample for powder X-ray diffraction (PXRD) was prepared on a zero-background sample holder inside the glovebox to avoid the exposure of powder to oxygen and moisture. The powder was transferred to a sample holder, which was covered with Kapton film and sealed using vacuum grease. PXRD was carried out using Rigaku XtaLAB Synergy-S diffractometer with HyPix-6000He Hybrid Photon Counting detector using Cu Kα($\lambda = 1.5406$ Å) radiation. The PXRD of samples was performed at a scanning speed of 1.16 °/min within the 2θ range of 10-50°.

Scanning electron microscope (SEM) images were obtained using a JEOL JSM-IT800 electron microscope (FE-SEM). Approximately 20 mg of sample powder was pressed in a 6 mm diameter stainless-steel mold at 300 MPa inside an argon-filled glovebox. The obtained pellet was thenplaced on the carbon tape in a vacuum-sealed sample holder. The sample holder was transferred into the exchange chamber of the JEOL JSM-IT800 and evacuated to ensure no air contamination on the pellets. An accelerating voltage of 5 kV was used and the SEM images were taken at the magnification of x 5.00 k for the acquisition time of 1 minute each.

Solid-state NMR experiments were carried out with an 11.75-T magnet and a 2.5-mm Bruker HXY probe. The samples were packed in 2.5-mm zirconia rotors and spun at the speed of 25 kHz. The ^{6}Li and ^{7}Li NMR spectra were obtained with single-pulse experiments with a flipping angle of 90 degrees. The ^{6}Li and ^{7}Li shifts were referenced to solid LiCl at -1.1 ppm. ^{7}Li T_1 was measured by using an inversion recovery pulse sequence. ^{31}P NMR spectra were collected using spin-echo experiments, and the ^{31}P shifts were referenced to 85% H_3PO_4 at 0 ppm. Raman spectra were collected using a Horiba JY LabRam HR Evolution Raman Spectrograph with a 633 nm excitation laser with a grating size of 1800 gr mm^{-1}.

4.3. Impedance measurements

The prepared pellet samples for both Li_3PS_4 and $3Li_3PS_4$:LiBr series were sandwiched between two indium foils as blocking electrodes and assembled into an in-house built 6mm dia cylindrical cell. Electrochemical impedance spectroscopy (EIS) was performed using a Gamry Reference 600+ in the frequency range of 0.1 Hz to 5 MHz. The bulk resistance was extracted from the Nyquist plot on EIS using an equivalent circuit model and the conductivity was calculated using **Equation 1**. Variable temperature EIS (VT-EIS) measurement was performed using a Biologic-SP300 in the CSZ microclimate chamber for heating and the activation energy was calculated using the Arrhenius-type equation.[42]

4.4. DC polarization

To measure the electronic conductivity, the DC polarization method was used.[43] In-house built split cells (diameter = 10 mm) using PEEK insulating cylinder and stainless-steel plungers as current collectors and ion-blocking electrodes were used.

4.5. Symmetric cycling

In-house-built PEEK split cells with stainless-steel plungers as current collectors were utilized for both critical current density (CCD) and extended symmetric cycling. 120 mg of SE was pressed at 300 MPa, placed between 0.1 mm thick Li foil (1/4 inch diameter), and cycled at 5 MPa stack pressure.[78] Cycling involved 30-minute currents in alternating directions with 5-minute breaks. In CCD tests, used current density increased by 0.02 mA cm^{-2} per cycle until cell shorting.

4.6. ASSB Assembly

The same PEEK split cells as described in the earlier section were employed for the assembly of ASSB half-cells. For cyclic voltammetry (CV) and galvanostatic cycling employing carbon-composite half-cells, initially, 100 mg of SE was pressed in the split cells at 300 MPa for 10 s. Subsequently, approximately 12 mg of the manually mixed 3SE:Carbon black (carbon is Super P) composite was uniformly spread onto one surface of the pellet and pressed at 300 MPa for 10 s. On the other side of the pellet, a piece of In foil measuring 5/16 inch diameter and 0.1 mm thickness, weighing ~32 mg was placed onto the pellet followed by Li foil with a diameter of 3/16 inch diameter and weighing approximately 1 mg. The cell was sealed using vacuum grease and then cycled under ~30 MPa stack pressure at 22 ℃. For CV measurements, a scan rate of 0.2 mV s^{-1} was used within a voltage range of 0 – 4 V *vs.* Li-In. A current density of 0.064 mA cm^{-2} was employed for the cells to cycle galvanostatically within the voltage window 0 – 4 V *vs* Li-In. For TiS_2:2SE half-cells, TiS_2 (Sigma, 99.9 %) was first dried at 200 ℃ for 12 hours to get rid of any adsorbed H_2O followed by planetary milling for 5 h at 300 RPM to decrease particle size.[79] Subsequently, the composite cathode was then manually mixed with Li_3PS_4 or $3Li_3PS_4$:LiBr in a 1:2 (TiS_2:SE) mass ratio using a mortar and pestle for 10 minutes. First, 100 mg of SE was pressed at 300 MPa for 10 seconds. Then, around 12 mg of catholyte was evenly distributed on one side of the pellet, corresponding to an aerial loading of approximately 1.25 mAh cm^{-2}, and pressed at 300 MPa for 10 seconds. On the opposite side of the pellet, a piece of indium foil (with a diameter of 5/16 inches) weighing roughly 32 mg was placed followed by Li foil (with a diameter of 3/16 inches) weighing about 1 mg. After sealing with vacuum grease, cells were cycled under ~30 MPa stack pressure at 22 ℃ between 1 – 2.5 V *vs.* Li-In.

Supporting Information

Supporting Information is available from the Wiley Online Library or from the authors.

Acknowledgment:

The authors acknowledge the support from the National Science Foundation under grant no. DMR-1847038 and from the NSF MRSEC program (NSF DMR-1720139). All solid-state NMR experiments were performed at the National High Magnetic Field Laboratory, which is supported by National Science Foundation Cooperative Agreement Nos. DMR-1644779 and DMR-2128556*.

Conflict of Interest:

The authors declare no conflict of interest.

Data Availability Statement

The data that supports this manuscript will be available upon reasonable request.

References:

(1) Sun, Y.; Liu, N.; Cui, Y. Promises and Challenges of Nanomaterials for Lithium-Based Rechargeable Batteries. *Nat. Energy* **2016**, *1* (7), 1–12. https://doi.org/10.1038/nenergy.2016.71.

(2) Chen, Y.; Kang, Y.; Zhao, Y.; Wang, L.; Liu, J.; Li, Y.; Liang, Z.; He, X.; Li, X.; Tavajohi, N.; Li, B. A Review of Lithium-Ion Battery Safety Concerns: The Issues, Strategies, and Testing Standards. *J. Energy Chem.* **2021**, *59*, 83–99. https://doi.org/10.1016/j.jechem.2020.10.017.

(3) Richards, W. D.; Miara, L. J.; Wang, Y.; Kim, J. C.; Ceder, G. Interface Stability in Solid-State Batteries. *Chem. Mater.* **2016**, *28* (1), 266–273. https://doi.org/10.1021/acs.chemmater.5b04082.

(4) Boaretto, N.; Garbayo, I.; Valiyaveettil-SobhanRaj, S.; Quintela, A.; Li, C.; Casas-Cabanas, M.; Aguesse, F. Lithium Solid-State Batteries: State-of-the-Art and Challenges for Materials, Interfaces and Processing. *J. Power Sources* **2021**, *502*, 229919. https://doi.org/10.1016/j.jpowsour.2021.229919.

(5) Budde-Meiwes, H.; Drillkens, J.; Lunz, B.; Muennix, J.; Rothgang, S.; Kowal, J.; Sauer, D. U. A Review of Current Automotive Battery Technology and Future Prospects. *Proc. Inst. Mech. Eng. Part J. Automob. Eng.* **2013**, *227* (5), 761–776. https://doi.org/10.1177/0954407013485567.

(6) Richards, W. D.; Miara, L. J.; Wang, Y.; Kim, J. C.; Ceder, G. Interface Stability in Solid-State Batteries. *Chem. Mater.* **2016**, *28* (1), 266–273. https://doi.org/10.1021/acs.chemmater.5b04082.

(7) Nitta, N.; Wu, F.; Lee, J. T.; Yushin, G. Li-Ion Battery Materials: Present and Future. *Mater. Today* **2015**, *18* (5), 252–264. https://doi.org/10.1016/j.mattod.2014.10.040.

(8) Li, X.; Liang, J.; Yang, X.; Adair, K. R.; Wang, C.; Zhao, F.; Sun, X. Progress and Perspectives on Halide Lithium Conductors for All-Solid-State Lithium Batteries. *Energy Environ. Sci.* **2020**, *13* (5), 1429–1461. https://doi.org/10.1039/C9EE03828K.

(9) Liu, Z.; Fu, W.; Payzant, E. A.; Yu, X.; Wu, Z.; Dudney, N. J.; Kiggans, J.; Hong, K.; Rondinone, A. J.; Liang, C. Anomalous High Ionic Conductivity of Nanoporous β-Li_3PS_4. *J. Am. Chem. Soc.* **2013**, *135* (3), 975–978. https://doi.org/10.1021/ja3110895.

(10) Wang, S.; Bai, Q.; Nolan, A. M.; Liu, Y.; Gong, S.; Sun, Q.; Mo, Y. Lithium Chlorides and Bromides as Promising Solid-State Chemistries for Fast Ion Conductors with Good Electrochemical Stability. *Angew. Chem. Int. Ed Engl.* **2019**, *58* (24), 8039–8043. https://doi.org/10.1002/anie.201901938.

(11) Schlem, R.; Banik, A.; Ohno, S.; Suard, E.; Zeier, W. G. Insights into the Lithium Sub-Structure of Superionic Conductors Li_3YCl_6 and Li_3YBr_6. *Chem. Mater.* **2021**, *33* (1), 327–337. https://doi.org/10.1021/acs.chemmater.0c04352.

(12) Guo, Y.; Wu, S.; He, Y.-B.; Kang, F.; Chen, L.; Li, H.; Yang, Q.-H. Solid-State Lithium Batteries: Safety and Prospects. *eScience* **2022**, *2* (2), 138–163. https://doi.org/10.1016/j.esci.2022.02.008.

(13) Budde-Meiwes, H.; Drillkens, J.; Lunz, B.; Muennix, J.; Rothgang, S.; Kowal, J.; Sauer, D. U. A Review of Current Automotive Battery Technology and Future Prospects. *Proc. Inst. Mech. Eng. Part J. Automob. Eng.* **2013**, *227* (5), 761–776. https://doi.org/10.1177/0954407013485567.

(14) Gür, T. M. Review of Electrical Energy Storage Technologies, Materials and Systems: Challenges and Prospects for Large-Scale Grid Storage. *Energy Environ. Sci.* **2018**, *11* (10), 2696–2767. https://doi.org/10.1039/C8EE01419A.

(15) Bachman, J. C.; Muy, S.; Grimaud, A.; Chang, H.-H.; Pour, N.; Lux, S. F.; Paschos, O.; Maglia, F.; Lupart, S.; Lamp, P.; Giordano, L.; Shao-Horn, Y. Inorganic Solid-State Electrolytes for Lithium Batteries: Mechanisms and Properties Governing Ion Conduction. *Chem. Rev.* **2016**, *116* (1), 140–162. https://doi.org/10.1021/acs.chemrev.5b00563.

(16) Zhao, W.; Yi, J.; He, P.; Zhou, H. Solid-State Electrolytes for Lithium-Ion Batteries: Fundamentals, Challenges and Perspectives. *Electrochem. Energy Rev.* **2019**, *2* (4), 574–605. https://doi.org/10.1007/s41918-019-00048-0.

(17) Patel, S. V.; Banerjee, S.; Liu, H.; Wang, P.; Chien, P.-H.; Feng, X.; Liu, J.; Ong, S. P.; Hu, Y.-Y. Tunable Lithium-Ion Transport in Mixed-Halide Argyrodites $Li_{6-x}PS_{5-x}ClBr_x$: An

Unusual Compositional Space. *Chem. Mater.* **2021**, *33* (4), 1435–1443. https://doi.org/10.1021/acs.chemmater.0c04650.

(18) Tatsumisago, M.; Hayashi, A. Superionic Glasses and Glass–Ceramics in the Li_2S–P_2S_5 System for All-Solid-State Lithium Secondary Batteries. *Solid State Ion.* **2012**, *225*, 342–345.

(19) Sakuda, A.; Hayashi, A.; Tatsumisago, M. Sulfide Solid Electrolyte with Favorable Mechanical Property for All-Solid-State Lithium Battery. *Sci. Rep.* **2013**, *3*, 2261.

(20) Suyama, M.; Kato, A.; Sakuda, A.; Hayashi, A.; Tatsumisago, M. Lithium Dissolution/Deposition Behavior with Li_3PS_4-LiI Electrolyte for All-Solid-State Batteries Operating at High Temperatures. *Electrochimica Acta* **2018**, *286*, 158–162.

(21) Kim, K.-H.; Martin, S. W. Structures and Properties of Oxygen-Substituted $Li_{10}SiP_2S_{12-x}O_x$ Solid-State Electrolytes. *Chem. Mater.* **2019**, *31* (11), 3984–3991. https://doi.org/10.1021/acs.chemmater.9b00505.

(22) Neveu, A.; Pelé, V.; Jordy, C.; Pralong, V. Exploration of Li–P–S–O Composition for Solid-State Electrolyte Materials Discovery. *J. Power Sources* **2020**, *467*, 228250. https://doi.org/10.1016/j.jpowsour.2020.228250.

(23) Tsujimura, T.; Ito, S.; Yoshida, K.; Higashiyama, Y.; Aihara, Y.; Machida, N.; Park, Y.; Im, D. Synthesis and Characterization of Low-Temperature Lithium-Ion Conductive Phase of LiX (X=Cl, Br)-Li_3PS_4 Solid Electrolytes. *Solid State Ion.* **2022**, *383*, 115970. https://doi.org/10.1016/j.ssi.2022.115970.

(24) Rangasamy, E.; Liu, Z.; Gobet, M.; Pilar, K.; Sahu, G.; Zhou, W.; Wu, H.; Greenbaum, S.; Liang, C. An Iodide-Based $Li_7P_2S_8I$ Superionic Conductor. *J. Am. Chem. Soc.* **2015**, *137* (4), 1384–1387. https://doi.org/10.1021/ja508723m.

(25) Wang, P.; Liu, H.; Patel, S.; Feng, X.; Chien, P.-H.; Wang, Y.; Hu, Y.-Y. Fast Ion Conduction and Its Origin in $Li_{6-x}PS_{5-x}Br_{1+x}$. *Chem. Mater.* **2020**, *32* (9), 3833–3840. https://doi.org/10.1021/acs.chemmater.9b05331.

(26) Han, F.; Yue, J.; Zhu, X.; Wang, C. Suppressing Li Dendrite Formation in Li2S-P2S5 Solid Electrolyte by LiI Incorporation. *Adv. Energy Mater.* **2018**, *8* (18), 1703644. https://doi.org/10.1002/aenm.201703644.

(27) Feng, X.; Chien, P.-H.; Wang, Y.; Patel, S.; Wang, P.; Liu, H.; Immediato-Scuotto, M.; Hu, Y.-Y. Enhanced Ion Conduction by Enforcing Structural Disorder in Li-Deficient Argyrodites $Li_{6-x}PS_{5-x}Cl_{1+x}$. *Energy Storage Mater.* **2020**, *30*, 67–73. https://doi.org/10.1016/j.ensm.2020.04.042.

(28) Bonnick, P.; Niitani, K.; Nose, M.; Suto, K.; Arthur, T. S.; Muldoon, J. A High Performance All Solid State Lithium Sulfur Battery with Lithium Thiophosphate Solid Electrolyte. *J. Mater. Chem. A* **2019**, *7* (42), 24173–24179. https://doi.org/10.1039/C9TA06971B.

(29) Wang, G.; Dong, P.; Liang, B.; Lin, C.; Shen, X.; Dai, S.; Jiao, Q. An Amorphous Superionic Conductor $Li_3PS_{4-x}LiBr$ with High Conductivity and Good Air Stability by Halogen Incorporation. *J. Am. Ceram. Soc.* **2022**, *105* (12), 7751–7759. https://doi.org/10.1111/jace.18704.

(30) Pan, L.; Zhang, L.; Ye, A.; Chi, S.; Zou, Z.; He, B.; Chen, L.; Zhao, Q.; Wang, D.; Shi, S. Revisiting the Ionic Diffusion Mechanism in Li_3PS_4 via the Joint Usage of Geometrical Analysis and Bond Valence Method. *J. Materiomics* **2019**, *5* (4), 688–695. https://doi.org/10.1016/j.jmat.2019.04.010.

(31) Levin, I. NIST Inorganic Crystal Structure Database (ICSD), **2020**. https://doi.org/10.18434/M32147.

(32) Li, X.; Deck, M.; Hu, Y.-Y. Solid-State NMR and EPR Characterization of Transition-Metal Oxides for Electrochemical Energy Storage. In *Transition Metal Oxides for Electrochemical Energy Storage*; John Wiley & Sons, Ltd, 2022; pp 299–318. https://doi.org/10.1002/9783527817252.ch12.

(33) Gamon, J.; Dyer, M. S.; Duff, B. B.; Vasylenko, A.; Daniels, L. M.; Zanella, M.; Gaultois, M. W.; Blanc, F.; Claridge, J. B.; Rosseinsky, M. J. Li4.3AlS3.3Cl0.7: A Sulfide–Chloride Lithium Ion Conductor with Highly Disordered Structure and Increased Conductivity. *Chem. Mater.* **2021**, *33* (22), 8733–8744. https://doi.org/10.1021/acs.chemmater.1c02751.

(34) Eckert, H.; Zhang, Z.; Kennedy, J. H. Structural Transformation of Non-Oxide Chalcogenide Glasses. The Short-Range Order of Lithium Sulfide (Li_2S)-Phosphorus Pentasulfide (P_2S_5) Glasses Studied by Quantitative Phosphorus-31, Lithium-6, and Lithium-7 High-Resolution Solid-State NMR. *Chem. Mater.* **1990**, *2* (3), 273–279. https://doi.org/10.1021/cm00009a017.

(35) Gobet, M.; Greenbaum, S.; Sahu, G.; Liang, C. Structural Evolution and Li Dynamics in Nanophase Li_3PS_4 by Solid-State and Pulsed-Field Gradient NMR. *Chem. Mater.* **2014**, *26* (11), 3558–3564. https://doi.org/10.1021/cm5012058.

(36) Chi, X.; Zhang, Y.; Hao, F.; Kmiec, S.; Dong, H.; Xu, R.; Zhao, K.; Ai, Q.; Terlier, T.; Wang, L.; Zhao, L.; Guo, L.; Lou, J.; Xin, H. L.; Martin, S. W.; Yao, Y. An Electrochemically Stable Homogeneous Glassy Electrolyte Formed at Room Temperature for All-Solid-State Sodium Batteries. *Nat. Commun.* **2022**, *13* (1), 2854. https://doi.org/10.1038/s41467-022-30517-y.

(37) Popovic, J.; Brandell, D.; Ohno, S.; B. Hatzell, K.; Zheng, J.; Hu, Y.-Y. Polymer-Based Hybrid Battery Electrolytes: Theoretical Insights, Recent Advances and Challenges. *J. Mater. Chem. A* **2021**, *9* (10), 6050–6069. https://doi.org/10.1039/D0TA11679C.

(38) Wu, N.; Chien, P.; Qian, Y.; Li, Y.; Xu, H.; Grundish, N. S.; Xu, B.; Jin, H.; Hu, Y.; Yu, G.; Goodenough, J. B. Enhanced Surface Interactions Enable Fast Li^+ Conduction in Oxide/Polymer Composite Electrolyte. *Angew. Chem.* **2020**, *132* (10), 4160–4166. https://doi.org/10.1002/ange.201914478.

(39) Miura, A.; Rosero-Navarro, N. C.; Sakuda, A.; Tadanaga, K.; Phuc, N. H. H.; Matsuda, A.; Machida, N.; Hayashi, A.; Tatsumisago, M. Liquid-Phase Syntheses of Sulfide Electrolytes for

All-Solid-State Lithium Battery. *Nat. Rev. Chem.* **2019**, *3* (3), 189–198. https://doi.org/10.1038/s41570-019-0078-2.

(40) Lunghammer, S.; Ma, Q.; Rettenwander, D.; Hanzu, I.; Tietz, F.; Wilkening, H. M. R. Bulk and Grain-Boundary Ionic Conductivity in Sodium Zirconophosphosilicate $Na_3Zr_2(SiO_4)_2PO_4$ (NASICON). *Chem. Phys. Lett.* **2018**, *701*, 147–150. https://doi.org/10.1016/j.cplett.2018.04.037.

(41) Liu, Z.; Fu, W.; Payzant, E. A.; Yu, X.; Wu, Z.; Dudney, N. J.; Kiggans, J.; Hong, K.; Rondinone, A. J.; Liang, C. Anomalous High Ionic Conductivity of Nanoporous β-Li_3PS_4. *J. Am. Chem. Soc.* **2013**, *135* (3), 975–978. https://doi.org/10.1021/ja3110895.

(42) Gao, Y.; Nolan, A. M.; Du, P.; Wu, Y.; Yang, C.; Chen, Q.; Mo, Y.; Bo, S.-H. Classical and Emerging Characterization Techniques for Investigation of Ion Transport Mechanisms in Crystalline Fast Ionic Conductors. *Chem. Rev.* **2020**, *120* (13), 5954–6008. https://doi.org/10.1021/acs.chemrev.9b00747.

(43) Ohno, S.; Rosenbach, C.; Dewald, G. F.; Janek, J.; Zeier, W. G. Linking Solid Electrolyte Degradation to Charge Carrier Transport in the Thiophosphate-Based Composite Cathode toward Solid-State Lithium-Sulfur Batteries. *Adv. Funct. Mater.* **2021**, *31* (18), 2010620. https://doi.org/10.1002/adfm.202010620.

(44) Zeng, Y.; Ouyang, B.; Liu, J.; Byeon, Y.-W.; Cai, Z.; Miara, L. J.; Wang, Y.; Ceder, G. High-Entropy Mechanism to Boost Ionic Conductivity. *Science* **2022**, *378* (6626), 1320–1324. https://doi.org/10.1126/science.abq1346.

(45) Banerjee, S.; Holekevi Chandrappa, M. L.; Ong, S. P. Role of Critical Oxygen Concentration in the β-$Li_3PS_{4-x}O_x$ Solid Electrolyte. *ACS Appl. Energy Mater.* **2022**, *5* (1), 35–41. https://doi.org/10.1021/acsaem.1c03795.

(46) L. Ndeugueu, J.; Aniya, M. On the Power Law Behavior of the A.C. Conductivity in Li Ion Conducting Perovskites. *J. Phys. Soc. Jpn.* **2010**, *79* (Suppl.A), 72–75. https://doi.org/10.1143/JPSJS.79SA.72.

(47) Hanghofer, I.; Brinek, M.; Eisbacher, S. L.; Bitschnau, B.; Volck, M.; Hennige, V.; Hanzu, I.; Rettenwander, D.; Wilkening, H. M. R. Substitutional Disorder: Structure and Ion Dynamics of the Argyrodites Li_6PS_5Cl, Li_6PS_5Br and Li_6PS_5I. *Phys. Chem. Chem. Phys.* **2019**, *21* (16), 8489–8507. https://doi.org/10.1039/C9CP00664H.

(48) Kamishima, O.; Iwai, Y.; Kawamura, J. Small Power-Law Dependence of Ionic Conductivity and Diffusional Dimensionality in β-Alumina. *Solid State Ion.* **2015**, *281*, 89–95. https://doi.org/10.1016/j.ssi.2015.09.011.

(49) Sidebottom, D. L. *Colloquium* : Understanding Ion Motion in Disordered Solids from Impedance Spectroscopy Scaling. *Rev. Mod. Phys.* **2009**, *81* (3), 999–1014. https://doi.org/10.1103/RevModPhys.81.999.

(50) Sidebottom, D. L. Dimensionality Dependence of the Conductivity Dispersion in Ionic Materials. *Phys. Rev. Lett.* **1999**, *83* (5), 983–986. https://doi.org/10.1103/PhysRevLett.83.983.

(51) Deck, M. J.; Hu, Y.-Y. Leveraging Local Structural Disorder for Enhanced Ion Transport. *J. Mater. Res.* **2023**, *38* (10), 2631–2644. https://doi.org/10.1557/s43578-023-01023-8.

(52) Botros, M.; Janek, J. Embracing Disorder in Solid-State Batteries. *Science* **2022**, *378* (6626), 1273–1274. https://doi.org/10.1126/science.adf3383.

(53) Sarkar, S.; Thangadurai, V. Critical Current Densities for High-Performance All-Solid-State Li-Metal Batteries: Fundamentals, Mechanisms, Interfaces, Materials, and Applications. *ACS Energy Lett.* **2022**, *7* (4), 1492–1527. https://doi.org/10.1021/acsenergylett.2c00003.

(54) Flatscher, F.; Philipp, M.; Ganschow, S.; R. Wilkening, H. M.; Rettenwander, D. The Natural Critical Current Density Limit for $Li_7La_3Zr_2O_{12}$ Garnets. *J. Mat*

er. Chem. A **2020**, *8* (31), 15782–15788. https://doi.org/10.1039/C9TA14177D.

(55) Lu, Y.; Zhao, C.; Yuan, H.; Cheng, X.; Huang, J.; Zhang, Q. Critical Current Density in Solid-State Lithium Metal Batteries: Mechanism, Influences, and Strategies. *Adv. Funct. Mater.* **2021**, *31* (18), 2009925. https://doi.org/10.1002/adfm.202009925.

(56) Dewald, G. F.; Ohno, S.; Kraft, M. A.; Koerver, R.; Till, P.; Vargas-Barbosa, N. M.; Janek, J.; Zeier, W. G. Experimental Assessment of the Practical Oxidative Stability of Lithium Thiophosphate Solid Electrolytes. *Chem. Mater.* **2019**, *31* (20), 8328–8337. https://doi.org/10.1021/acs.chemmater.9b01550.

(57) Peljo, P.; H. Girault, H. Electrochemical Potential Window of Battery Electrolytes: The HOMO–LUMO Misconception. *Energy Environ. Sci.* **2018**, *11* (9), 2306–2309. https://doi.org/10.1039/C8EE01286E.

(58) Zhu, Y.; He, X.; Mo, Y. Origin of Outstanding Stability in the Lithium Solid Electrolyte Materials: Insights from Thermodynamic Analyses Based on First-Principles Calculations. *ACS Appl. Mater. Interfaces* **2015**, *7* (42), 23685–23693. https://doi.org/10.1021/acsami.5b07517.

(59) Wang, S.; Wu, X.; Liang, Y.; Xu, Y.; Guan, S.; Wen, K.; Miao, X.; Liang, Y.; He, H.; Lin, Y.; Shen, Y.; Nan, C.-W. Facile Synthesis of Lithium Argyrodite Li5.5PS4.5Br1.5 with High Ionic Conductivity for All-Solid-State Batteries. *Front. Chem. Eng.* **2022**, *4*.

(60) Tan, D. H. S.; Wu, E. A.; Nguyen, H.; Chen, Z.; Marple, M. A. T.; Doux, J.-M.; Wang, X.; Yang, H.; Banerjee, A.; Meng, Y. S. Elucidating Reversible Electrochemical Redox of Li_6PS_5Cl Solid Electrolyte. *ACS Energy Lett.* **2019**, *4* (10), 2418–2427. https://doi.org/10.1021/acsenergylett.9b01693.

(61) Schwietert, T. K.; Arszelewska, V. A.; Wang, C.; Yu, C.; Vasileiadis, A.; de Klerk, N. J. J.; Hageman, J.; Hupfer, T.; Kerkamm, I.; Xu, Y.; van der Maas, E.; Kelder, E. M.; Ganapathy, S.; Wagemaker, M. Clarifying the Relationship between Redox Activity and Electrochemical Stability in Solid Electrolytes. *Nat. Mater.* **2020**, *19* (4), 428–435. https://doi.org/10.1038/s41563-019-0576-0.

(62) Tian, Y.; Shi, T.; D. Richards, W.; Li, J.; Chul Kim, J.; Bo, S.-H.; Ceder, G. Compatibility Issues between Electrodes and Electrolytes in Solid-State Batteries. *Energy Environ. Sci.* **2017**, *10* (5), 1150–1166. https://doi.org/10.1039/C7EE00534B.

(63) Han, F.; Zhu, Y.; He, X.; Mo, Y.; Wang, C. Electrochemical Stability of $Li_{10}GeP_2S_{12}$ and $Li_7La_3Zr_2O_{12}$ Solid Electrolytes. *Adv. Energy Mater.* **2016**, *6*, n/a-n/a. https://doi.org/10.1002/aenm.201501590.

(64) Wang, S.; Fang, R.; Li, Y.; Liu, Y.; Xin, C.; Richter, F. H.; Nan, C.-W. Interfacial Challenges for All-Solid-State Batteries Based on Sulfide Solid Electrolytes. *J. Materiomics* **2021**, *7* (2), 209–218. https://doi.org/10.1016/j.jmat.2020.09.003.

(65) Bui, A. D.; Choi, S.-H.; Choi, H.; Lee, Y.-J.; Doh, C.-H.; Park, J.-W.; Kim, B. G.; Lee, W.-J.; Lee, S.-M.; Ha, Y.-C. Origin of the Outstanding Performance of Dual Halide Doped $Li_7P_2S_8X$ (X = I, Br) Solid Electrolytes for All-Solid-State Lithium Batteries. *ACS Appl. Energy Mater.* **2021**, *4* (1), 1–8. https://doi.org/10.1021/acsaem.0c02321.

(66) Hakari, T.; Deguchi, M.; Mitsuhara, K.; Ohta, T.; Saito, K.; Orikasa, Y.; Uchimoto, Y.; Kowada, Y.; Hayashi, A.; Tatsumisago, M. Structural and Electronic-State Changes of a Sulfide Solid Electrolyte during the Li Deinsertion–Insertion Processes. *Chem. Mater.* **2017**, *29* (11), 4768–4774. https://doi.org/10.1021/acs.chemmater.7b00551.

(67) Takada, K.; Osada, M.; Ohta, N.; Inada, T.; Kajiyama, A.; Sasaki, H.; Kondo, S.; Watanabe, M.; Sasaki, T. Lithium Ion Conductive Oxysulfide, Li_3PO_4–Li_3PS_4. *Solid State Ion.* **2005**, *176* (31), 2355–2359. https://doi.org/10.1016/j.ssi.2005.03.023.

(68) Hakari, T.; Nagao, M.; Hayashi, A.; Tatsumisago, M. All-Solid-State Lithium Batteries with Li_3PS_4 Glass as Active Material. *J. Power Sources* **2015**, *293*, 721–725. https://doi.org/10.1016/j.jpowsour.2015.05.073.

(69) See, K.; Lumley, M.; Stucky, G.; Grey, C.; Seshadri, R. Reversible Capacity of Conductive Carbon Additives at Low Potentials: Caveats for Testing Alternative Anode Materials for Li-Ion Batteries. *J. Electrochem. Soc.* **2017**, *164*, A327–A333. https://doi.org/10.1149/2.0971702jes.

(70) Zhang, W.; Richter, F. H.; Culver, S. P.; Leichtweiss, T.; Lozano, J. G.; Dietrich, C.; Bruce, P. G.; Zeier, W. G.; Janek, J. Degradation Mechanisms at the $Li_{10}GeP_2S_{12}$/$LiCoO_2$ Cathode Interface in an All-Solid-State Lithium-Ion Battery. *ACS Appl. Mater. Interfaces* **2018**, *10* (26), 22226–22236. https://doi.org/10.1021/acsami.8b05132.

(71) Qu, J.; Xiao, J.; Wang, T.; Legut, D.; Zhang, Q. High Rate Transfer Mechanism of Lithium Ions in Lithium–Tin and Lithium–Indium Alloys for Lithium Batteries. *J. Phys. Chem. C* **2020**, *124* (45), 24644–24652. https://doi.org/10.1021/acs.jpcc.0c07880.

(72) Oh, D. Y.; Choi, Y. E.; Kim, D. H.; Lee, Y.-G.; Kim, B.-S.; Park, J.; Sohn, H.; Jung, Y. S. All-Solid-State Lithium-Ion Batteries with TiS_2 Nanosheets and Sulphide Solid Electrolytes. *J. Mater. Chem. A* **2016**, *4* (26), 10329–10335. https://doi.org/10.1039/C6TA01628F.

(73) Shin, B. R.; Nam, Y. J.; Kim, J. W.; Lee, Y.-G.; Jung, Y. S. Interfacial Architecture for Extra Li^+ Storage in All-Solid-State Lithium Batteries. *Sci. Rep.* **2014**, *4* (1), 5572. https://doi.org/10.1038/srep05572.

(74) Minnmann, P.; Quillman, L.; Burkhardt, S.; Richter, F. H.; Janek, J. Editors' Choice—Quantifying the Impact of Charge Transport Bottlenecks in Composite Cathodes of All-Solid-State Batteries. *J. Electrochem. Soc.* **2021**, *168* (4), 040537. https://doi.org/10.1149/1945-7111/abf8d7.

(75) Patel, S. V.; Truong, E.; Liu, H.; Jin, Y.; Chen, B. L.; Wang, Y.; Miara, L.; Kim, R.; Hu, Y.-Y. Interrupted Anion-Network Enhanced Li^+-Ion Conduction in $Li_{3+y}PO_4Iy$. *Energy Storage Mater.* **2022**, *51*, 88–96. https://doi.org/10.1016/j.ensm.2022.06.026.

(76) Feng, X.; Chien, P.-H.; Zhu, Z.; Chu, I.-H.; Wang, P.; Immediato-Scuotto, M.; Arabzadeh, H.; Ong, S. P.; Hu, Y.-Y. Studies of Functional Defects for Fast Na-Ion Conduction in $Na_{3-y}PS_{4-x}Cl_x$ with a Combined Experimental and Computational Approach. *Adv. Funct. Mater.* **2019**, *29* (9), 1807951. https://doi.org/10.1002/adfm.201807951.

(77) Zhang, D. L. Processing of Advanced Materials Using High-Energy Mechanical Milling. *Prog. Mater. Sci.* **2004**, *49* (3–4), 537–560.

(78) Doux, J.-M.; Nguyen, H.; Tan, D. H. S.; Banerjee, A.; Wang, X.; Wu, E. A.; Jo, C.; Yang, H.; Meng, Y. S. Stack Pressure Considerations for Room-Temperature All-Solid-State Lithium Metal Batteries. *Adv. Energy Mater.* **2020**, *10* (1), 1903253. https://doi.org/10.1002/aenm.201903253.

(79) Trevey, J. E.; Stoldt, C. R.; Lee, S.-H. High Power Nanocomposite TiS_2 Cathodes for All-Solid-State Lithium Batteries. *J. Electrochem. Soc.* **2011**, *158* (12), A1282. https://doi.org/10.1149/2.017112jes.

Upon mechanochemical milling β-Li_3PS_3 with LiBr to introduce local disorder on the nanoscale, the ionic conductivity increases more than four-fold with a decrease in E_a.

Tej P. Poudel, Michael J. Deck, Pengbo Wang, Yan-Yan Hu*

Transforming Li_3PS_4 via Halide Incorporation: A Path to Improved Ionic Conductivity and Stability in All-Solid-State Batteries

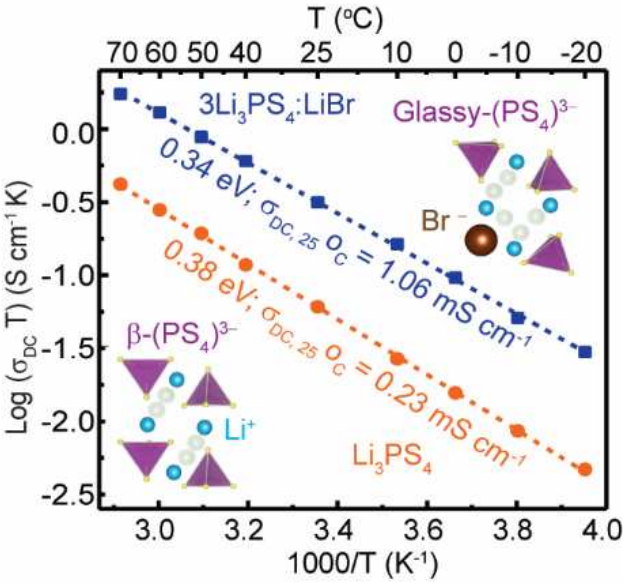

Transforming Li_3PS_4 via Halide Incorporation: A Path to Improved Ionic Conductivity and Stability in All-Solid-State Batteries

Tej P. Poudel,[1,2] Michael J. Deck,[2] Pengbo Wang,[2] Yan-Yan Hu[1,2,3,]*

1. Materials Science and Engineering, Florida State University, Tallahassee, FL, 32310, USA
2. Chemistry and Biochemistry, Florida State University, Tallahassee, FL, 32306, USA
3. National High Magnetic Field Laboratory, Tallahassee, FL, 32310, USA

Supporting Information

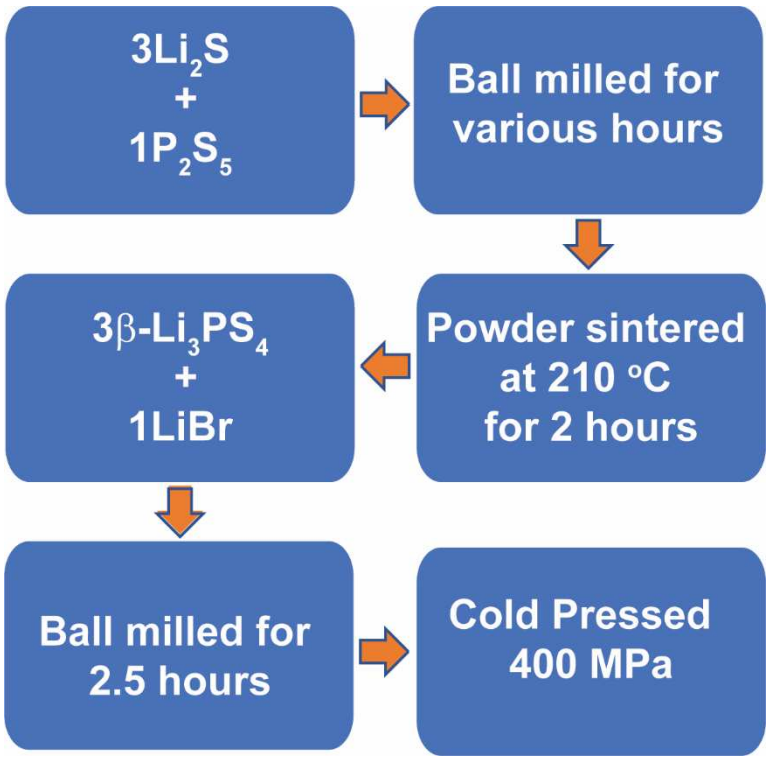

Figure S1. Schematic of two-stage ball milling for the synthesis of $3Li_3PS_4$:LiBr composite solid electrolyte.

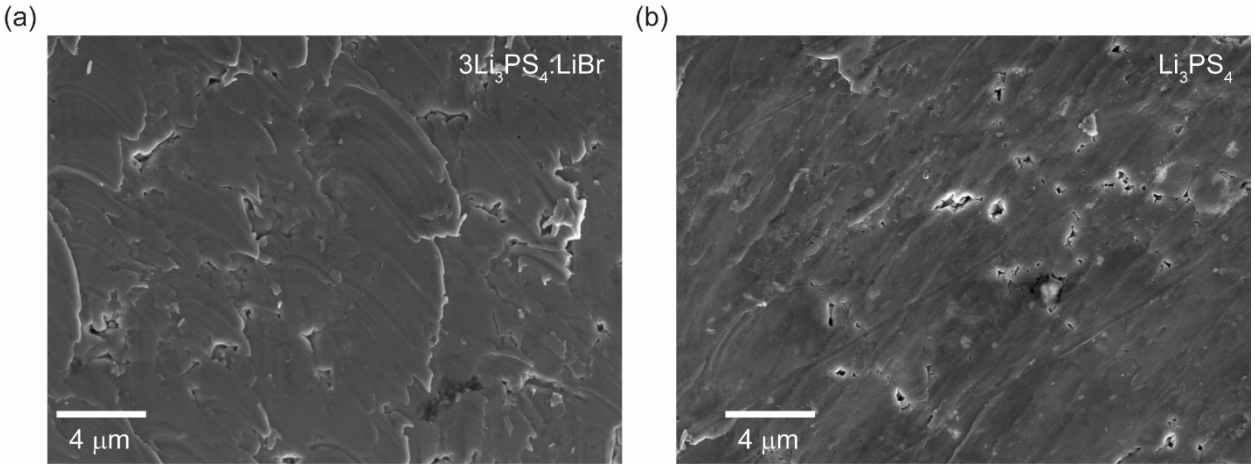

Figure S2. Scanning electron microscope images of (a) $3Li_3PS_4$:LiBr and (b) Li_3PS_4 SEs. Both $3Li_3PS_4$:LiBr and Li_3PS_4 have a similar grain/particle size distribution ranging from 0.5 μm to 2 μm.

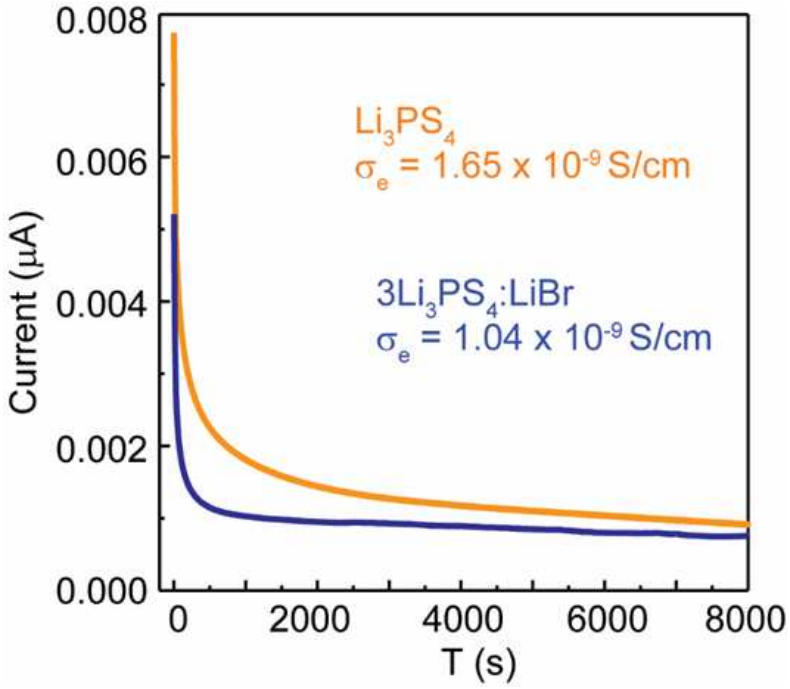

Figure S3. DC polarization measurement and the calculated electronic conductivity of LPS and 3LPS:LiBr SEs. There is a decrease in the electronic conductivity of LPS with LiBr incorporation.

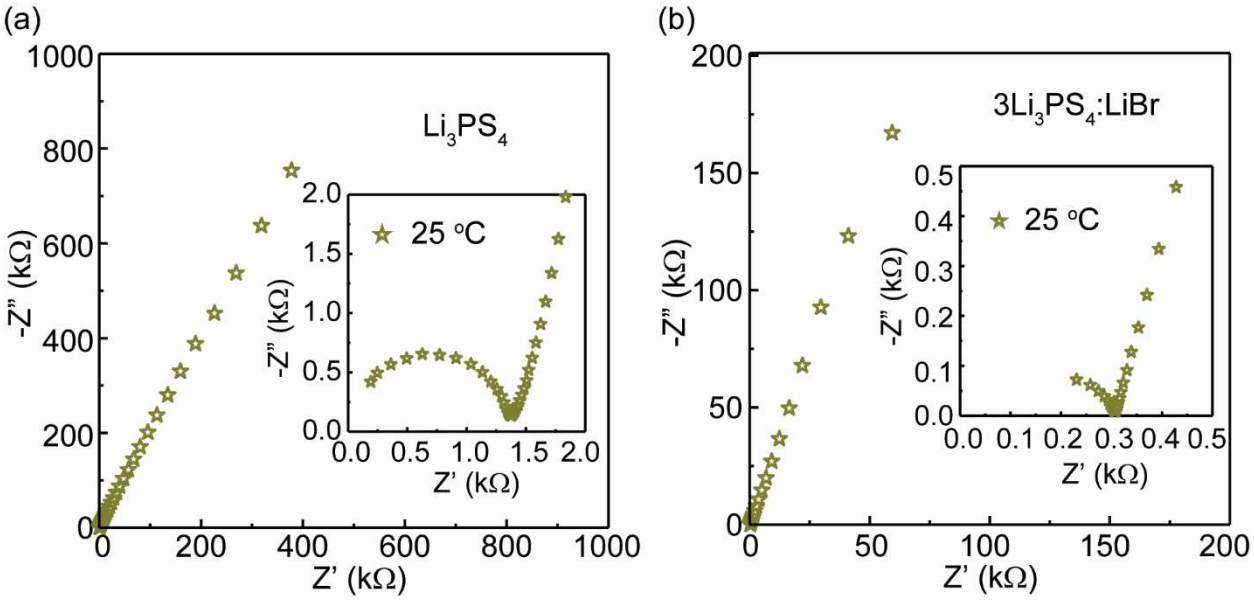

Figure S4. Room temperature Nyquist plots of (a) Li_3PS_4, (b) Li_3PS_4:LiBr, and their respective magnified view (insets).

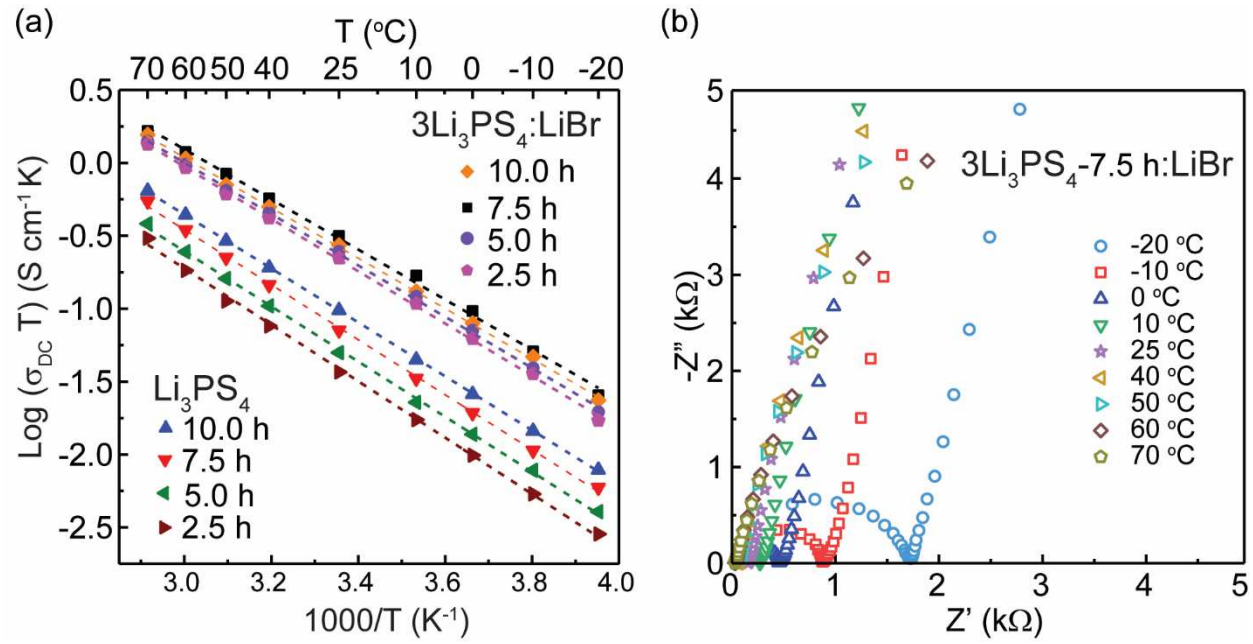

Figure S5. (a) Arrhenius-type plot of Li_3PS_4 and $3Li_3PS_4$:LiBr SEs, and (b) a representative temperature-dependent EIS Nyquist plots of $3Li_3PS_4$:1LiBr electrolyte milled for 7.5 hours.

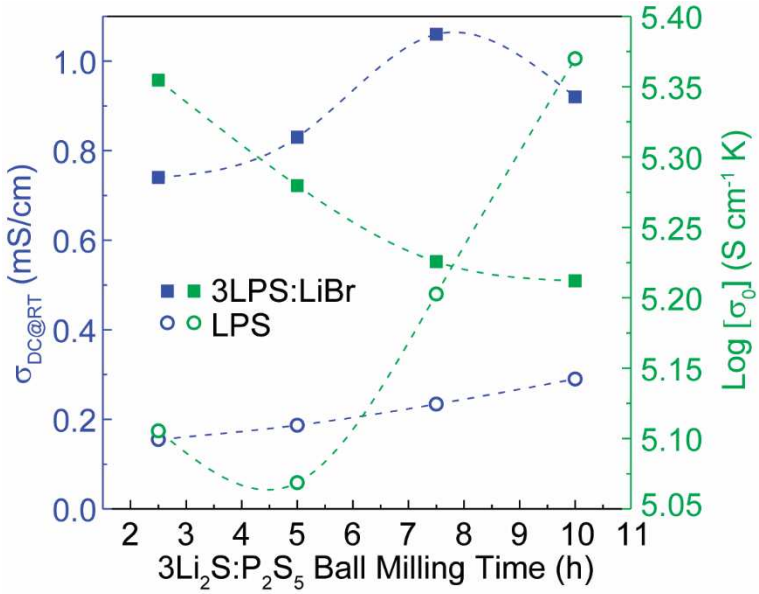

Figure S6. Comparison of conductivity of SEs with $3Li_2S$:P_2S_5 ball milling time vs the Arrhenius perfector (For all the $3Li_3PS_4$:LiBr electrolytes the second-stage ball milling time of 2.5 h was used).

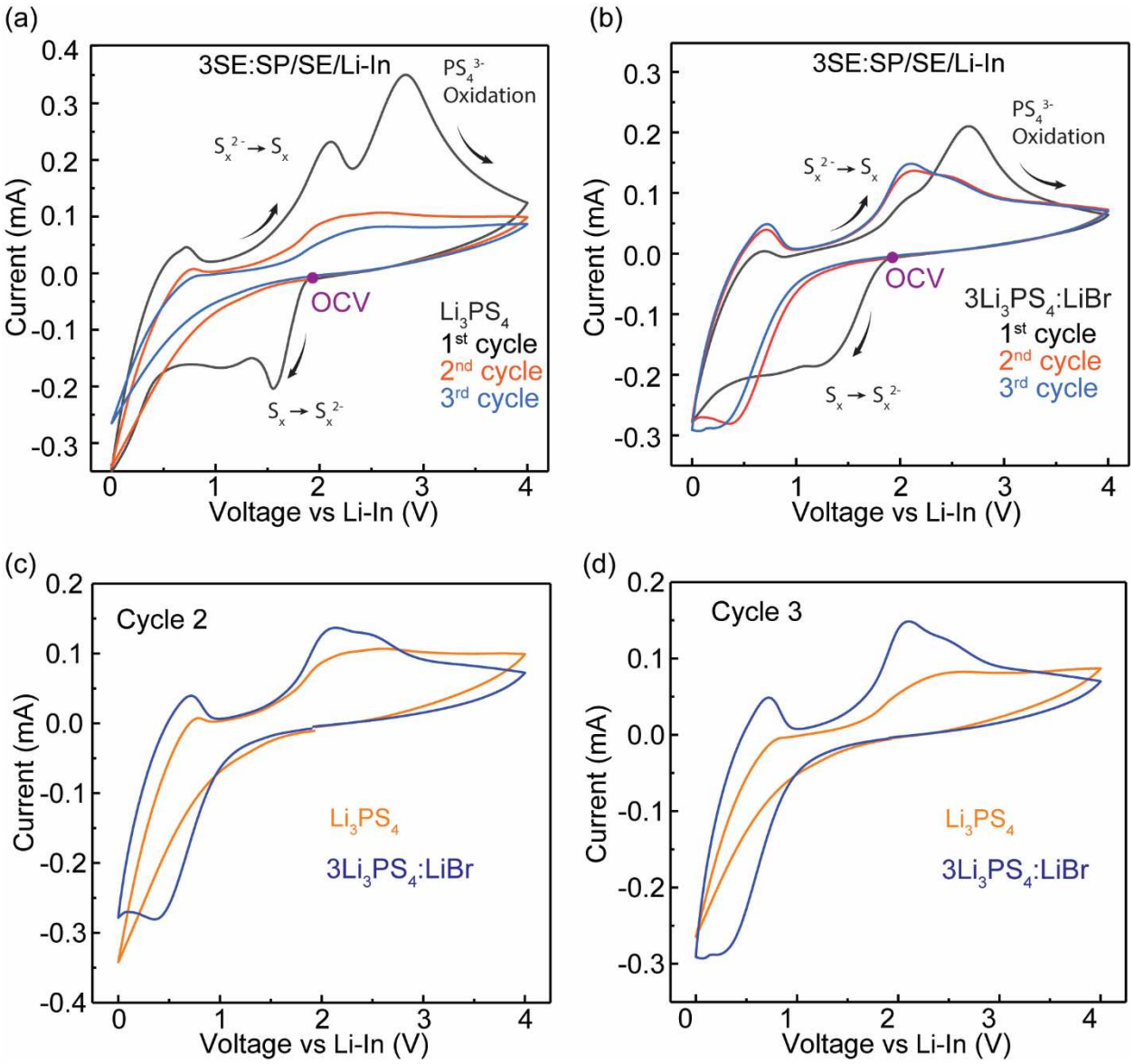

Figure S7. First three sweeps of cyclic voltammogram of (a) LPS (b) $3Li_3PS_4$:1LiBr SE. (c) and (d) shows the comparison of the 2nd and 3rd cycle of the cyclic voltammogram of both the SEs, respectively.

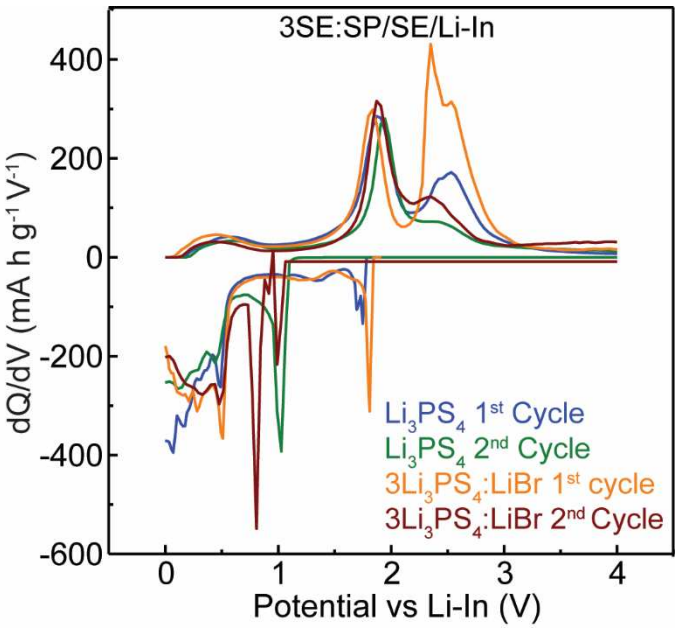

Figure S8. The comparison of the differential capacity of SE carbon-composite cells for the first and second cycles of galvanostatic cycling. Starting from the second cycle of both Li_3PS_4 and $3Li_3PS_4$:LiBr cells, the electrochemical window spans from ~1.0 V to ~2.2 V *vs*. Li-In. The preservation of the electrochemical window is evident even with the incorporation of LiBr into Li_3PS_4.

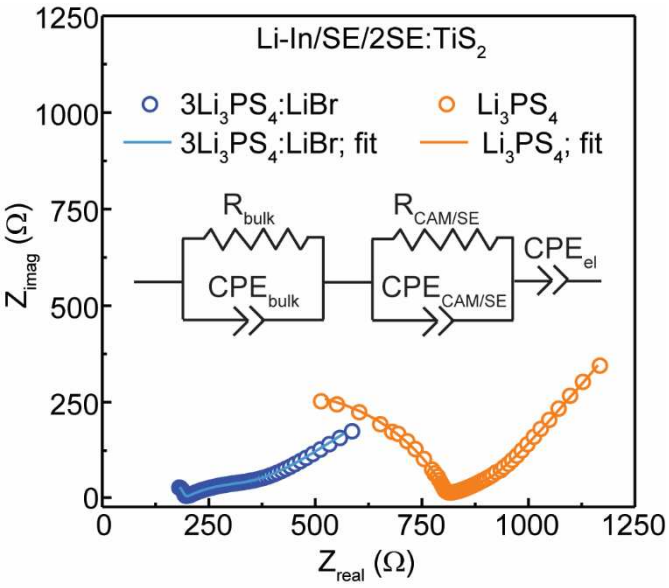

Figure S9. Nyquist plots of half-cells containing Li_3PS_4 and $3Li_3PS_4$:LiBr as solid electrolytes, TiS_2 as CAM, and Li-In as anode. The inset shows the corresponding equivalent circuit for both the cells. The first semicircle at high-frequency is attributed to bulk SE response, the second

semicircle at middle-frequency range is attributed to the CAM/SE interface response, and the low-frequency tail is attributed to the Li^+ diffusion into the electrodes.[34,70]

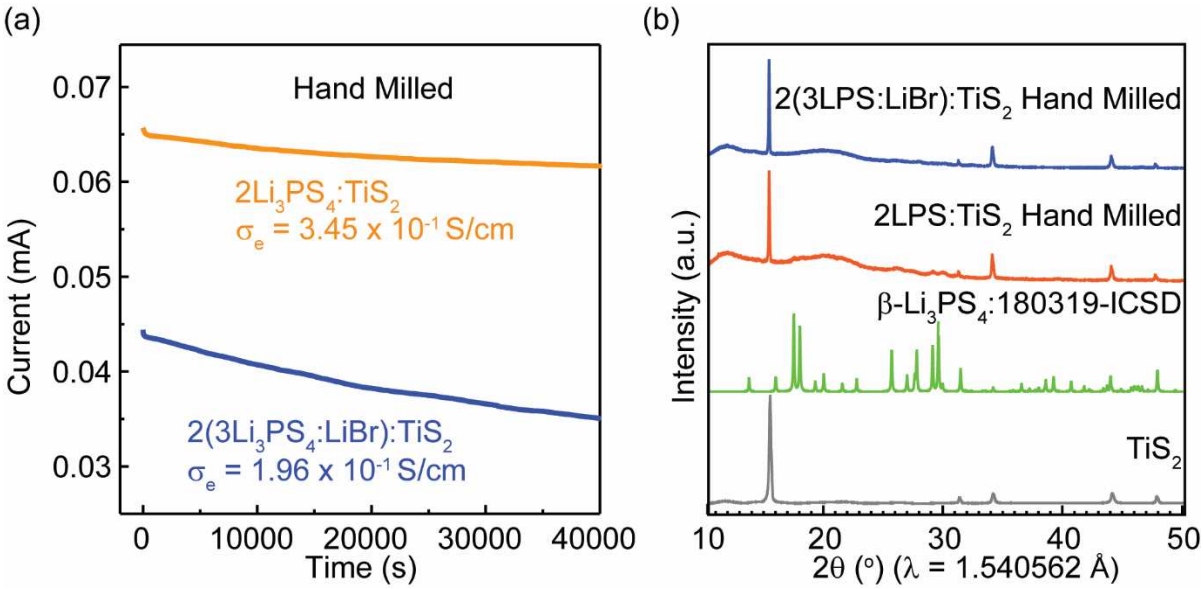

Figure S10. (a) DC polarization and (b) PXRD pattern of the hand-milled catholyte and comparison with TiS2 and β-Li_3PS_4. The electronic conductivity of $2Li_3PS_4$:TiS_2 is observed to be 3.45 x 10^{-1} S/cm whereas the electronic conductivity of $2(3Li_3PS_4$:LiBr):TiS_2 catholyte is observed to be 1.96 x 10^{-1} S/cm. The $2Li_3PS_4$:TiS_2 catholyte after hand milling shows the presence of both LPS and TiS_2 phases. However, The $2(3Li_3PS_4$:LiBr):TiS_2 catholyte after hand milling shows the presence of TiS_2 phase from XRD, which is because the $3Li_3PS_4$:LiBr electrolyte is observed to be glassy amorphous from **Figure 1** in the main text.

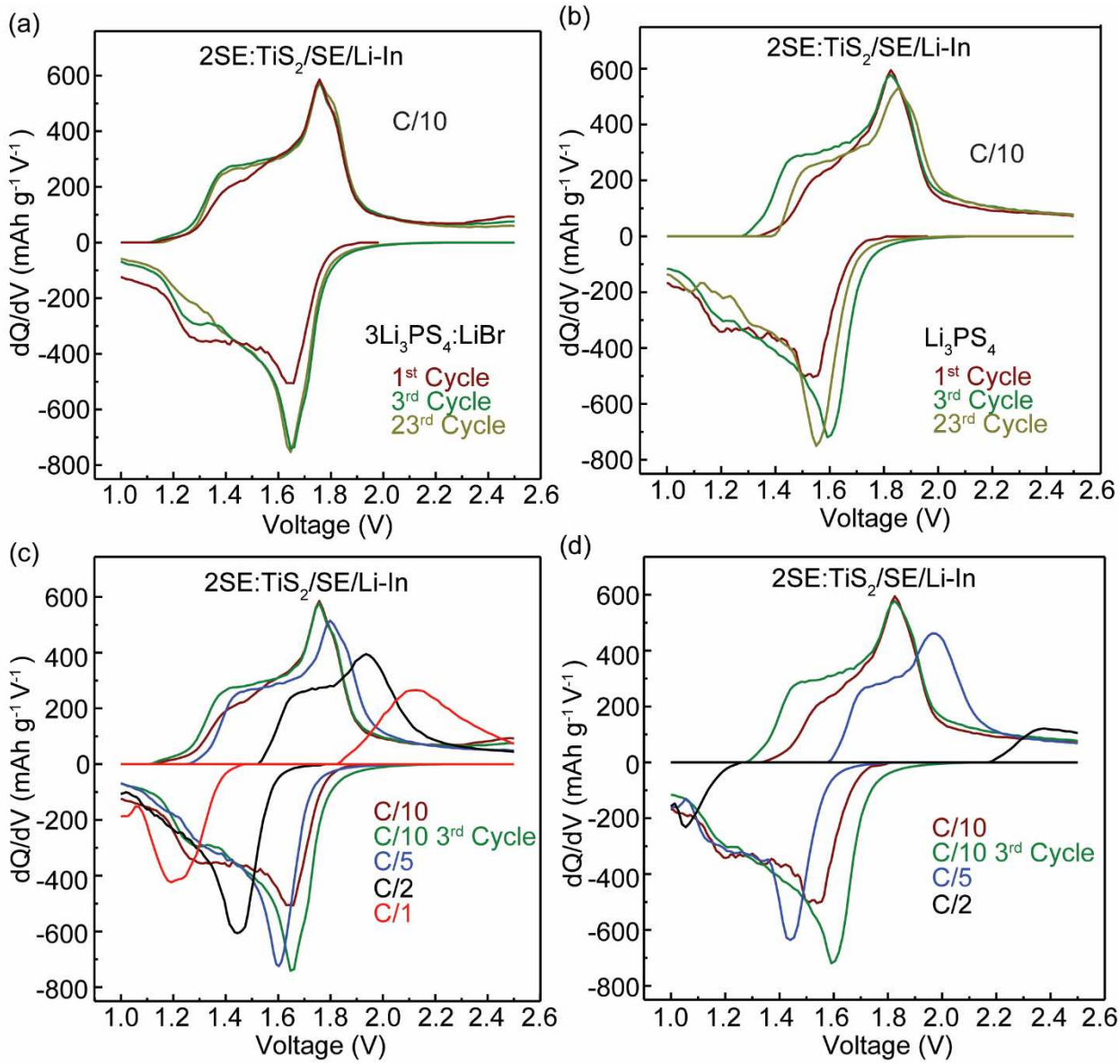

Figure S11. Differential capacity plots of selected cycles of (a) $3Li_3PS_4$:LiBr, and (b) Li_3PS_4 SEs at a charge-discharge rate of 0.1C. (c) and (d) shows the differential capacity plots of $3Li_3PS_4$:LiBr and Li_3PS_4 SEs at various charge-discharge rates. For both SEs the redox peak for $Ti^{3+/4+}$ is observed.

Table S3. ^{6}Li and ^{31}P quantitative analysis of each component in the percentage of the total (%). See the main text for the full discussion

Sample	^{6}Li (%)		^{31}P (%)		
	$3Li_3PS_4$:LiBr	Other phases	PS_4^{-3}	$P_2S_7^{-4}$	$P_2S_6^{-4}$
Li_3PS_4-BM-10h	81.4	18.6	100	0	0
$3Li_3PS_4$-BM-2.5h:LiBr	83.8	12.6	87.9	6.2	5.9
$3Li_3PS_4$-BM-7.5h:LiBr	100	0	96.5	1.5	2

Table S2. Summary of EIS analysis on Li_3PS_4 and $3Li_3PS_4$:LiBr including ionic conductivity, activation energy, and Arrhenius prefactor. For all the $3Li_3PS_4$:LiBr electrolytes the second-stage ball-milling time of 2.5 h was used.

Sample	$3Li_2S$:P_2S_5 (first-stage) ball-milling Time [h]	$\sigma_{DC,}$ 25 °C [mS/cm]	E_a[eV]	Log σ_0 [S cm^{-1} K]
Li_3PS_4	2.5	0.16	0.39	5.11
	5.0	0.19	0.38	5.07
	7.5	0.23	0.38	5.20
	10.0	0.29	0.38	5.37
$3Li_3PS_4$:LiBr	2.5	0.74	0.36	5.35
	5.0	0.83	0.35	5.28
	7.5	1.06	0.34	5.23

	10.0	0.92	0.34	5.21

Table S3. Summary of Nyquist plot analysis on Li-In/Li_3PS_4/2Li_3PS_4:TiS_2 and Li-In/3Li_3PS_4:LiBr/2(3Li_3PS_4:LiBr):TiS_2 half cells

Sample	R_{Bulk} [Ω]	CPE_{Bulk} [Ω^{-1} s]	$R_{CAM/SE}$ [Ω]	$CPE_{CAM/SE}$ [Ω^{-1} s]	CPE_{el} [Ω^{-1} s]
Li_3PS_4	810	1.7×10^{-9}	100	3.3×10^{-4}	8.0×10^{-4}
3Li_3PS_4:LiBr	173	5.2×10^{-4}	192	3.8×10^{-10}	4.5×10^{-3}